Data-driven synapse classification reveals a logic of glutamate receptor composition

Kristina D. Micheva[1]*, Anish K. Simhal[2], Jenna Schardt[3], Stephen J Smith[3,4]**,

Richard J. Weinberg[5]***, Scott F. Owen[1,6,7]****

[1]Department of Neurosurgery, Stanford University School of Medicine, Stanford, CA 94305

[2]Department of Medical Physics, Memorial Sloan Kettering Cancer Center, New York, NY 10065

[3]Allen Institute for Brain Science, Seattle, WA 98109

[4]Department of Molecular and Cellular Physiology, Stanford University School of Medicine, Stanford, CA 94305

[5]Department of Cell Biology and Physiology, University of North Carolina, Chapel Hill, NC 27514

[6]Wu Tsai Neurosciences Institute, Stanford University, Stanford, CA 94305

[7]Lead contact

*Correspondence: kmicheva@stanford.edu

**Correspondence: sjsmith@stanford.edu

***Correspondence: richard.weinberg@gmail.com

****Correspondence: sfowen@stanford.edu

Summary

The rich diversity of synapses facilitates the capacity of neural circuits to transmit, process and store information. Here, we used multiplex super-resolution proteometric imaging through array tomography to define features of single synapses in the adult mouse neocortex. We find that glutamatergic synapses cluster into subclasses that parallel the distinct biochemical and functional categories of receptor subunits: GluA1/4, GluA2/3 and GluN1/GluN2B. Two of these subclasses align with physiological expectations based on synaptic plasticity: large AMPAR-rich synapses may represent potentiated synapses, whereas small NMDAR-rich synapses suggest “silent” synapses. The NMDA receptor content of large synapses correlates with spine neck diameter, and thus the potential for coupling to the parent dendrite. Conjugate array tomography’s rigorous registration of immunofluorescence with electron microscopy provides validation for future super-resolution imaging studies in other systems. No barriers prevent generalization of this approach to other species, laying a foundation for future studies of human disorders and therapeutics.

Keywords: array tomography, immunofluorescence, electron microcopy, correlative microscopy, synapse, neocortex, NMDA, AMPA

Highlights

- Conjugate array tomography enables and validates single-synapse proteometry
- Glutamate receptor proteometry identifies subclasses of glutamatergic synapses
- Conjugate array tomography places synapse subclasses in ultrastructural context
- Subclasses align with established molecular correlates of functional plasticity

Graphical Abstract

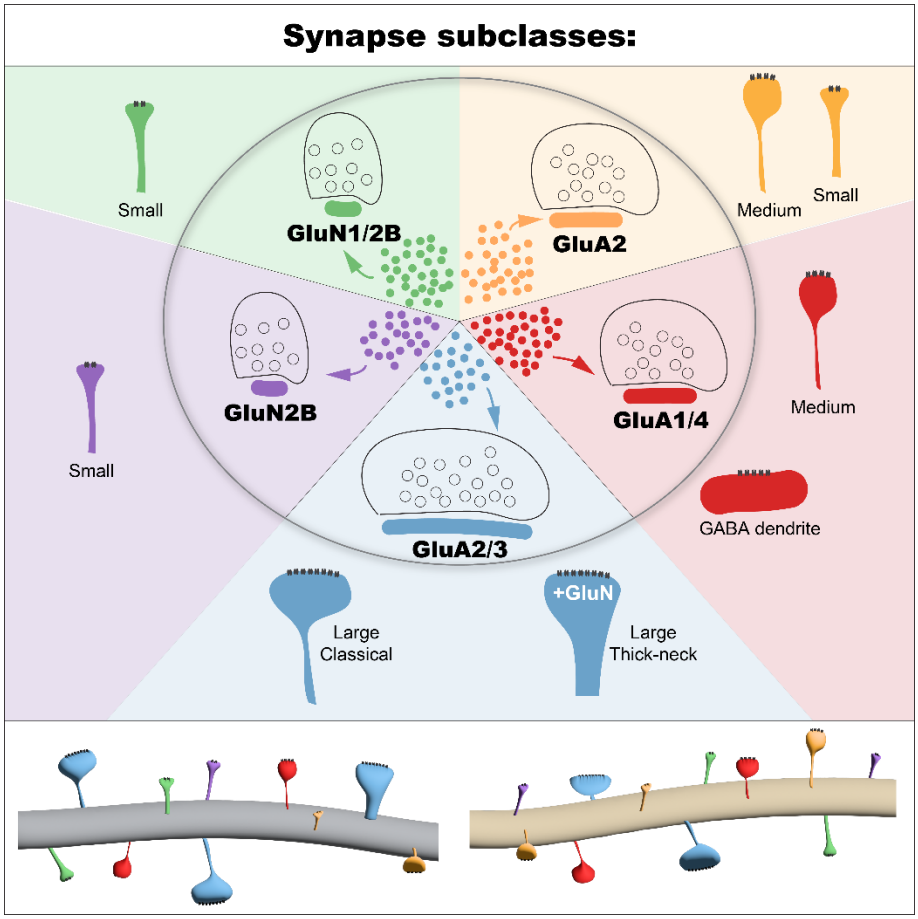

Abbreviations:

AMPAR: The α-amino-3-hydroxy-5-methyl-4-isoxazolepropionic acid receptor

NMDAR: The *N*-methyl D-aspartate receptor

GABA: gamma-aminobutyric acid

EM: Electron microscopy

SEM: Scanning electron microscopy

IF: Immunofluorescence

AT: Array tomography

PSD-95: Postsynaptic density protein 95

TeA: Temporal association cortex

UMAP: Uniform manifold approximation and projection

Introduction

Synapses display remarkable diversity in size, molecular composition, subcellular localization, and function[1–13] thus shaping the transmission and processing of information in neural circuits. Active regulation of synaptic strength associated with modifications in the size and composition of receptors is fundamental to memory storage and neuronal plasticity[14–28].

Even within a single tightly restricted anatomical region, the sizes of individual synaptic contacts show greater than tenfold variation, as do unitary transmission strengths[1–6]. The molecular composition of synapses is tightly orchestrated through brain development[29–34], and risk genes for prevalent neurological disorders including autism, epilepsy, and psychosis are heavily weighted towards synaptic function[35–40]. Quantitative, single-synapse-level profiling to define the logic underlying these synapse populations is therefore critical to understanding both normal and disordered brain development and function.

Here we introduce an approach for single-synapse population profiling based on conjugate array tomography (AT), which uses immunofluorescence followed by scanning EM on serial ultrathin sections to reveal both proteometry and tissue ultrastructure[41]. We apply conjugate AT to adult mouse Temporal Association cortex (TeA). Array tomography has unmatched capacity to bring both multiplexed super-resolution volume fluorescence and volume electron microscopy to bear on individual synapses[10,41–49], but has not yet been fully exploited for high-dimensional microproteometric analysis. Multi-channel immunofluorescence images enable quantitative sampling of the protein composition of single synapses, while electron microscopy allows precise quantification of the size, shape, and ultrastructural context of the same individual synapses. Machine-learning tools efficiently extract mechanistic insight from this rich, multi-dimensional data.

Of the hundreds of distinct proteins present at individual synapses[35,50–53], the proteins that most directly impact synaptic strength include neurotransmitter receptors and postsynaptic density scaffolds[12,41,51,54,55]. We therefore selected a set of proteins based on their direct role in generation of excitatory post-synaptic currents, and their relevance to activity-dependent plasticity and thus to memory storage[21,52,56]. These include four AMPA-type and two NMDA-type glutamate receptor subunits, along with the scaffold proteins PSD-95, gephyrin and synapsin 1/2, and the cell-type markers GABA and vesicular glutamate transporter 1. The tight three-dimensional registration of volume immunofluorescence and electron microscopy images in our data reveals important connections between ultrastructural and molecular features of individual synapses, and sheds new light on the rules governing the scaling of glutamate receptor content with synapse size and target cell identity.

Our analysis indicates that the myriad of diverse glutamatergic synapses in our neocortical target region can be clustered into a modest number of subclasses based on glutamate receptor expression. This clustering is robust even when only multi-channel immunofluorescence data is available, suggesting that this synapse classification rubric can be generally applied across experimental systems and areas of investigation. The logic of these subclasses can be readily interpreted in the context of distinct physiological roles. For example, large AMPAR-rich synapses suggest full potentiation, while small NMDAR-rich synapses that lack detectable AMPA receptors suggest functionally “silent” synapses. Volume electron microscopy reveals that ultrastructural features like spine head and neck diameter are better predictors of the proteometric content of individual synapses than pre- or postsynaptic parent neuron identity.

This method to profile the diversity of synapses promises to advance our basic understanding of brain development, circuit function, learning and memory. Furthermore, by

providing a quantitative rubric to characterize deficits in specific populations of synapses, we offer a valuable new tool to elucidate the synaptic basis of brain and memory disorders.

Results

Conjugate array tomography enables multiplex immunolabeling of ultrastructurally-identified synapses

We used multiplex immunolabeling and conjugate AT to explore the receptor composition and morphology of glutamatergic synapses in layers 2/3 of Temporal association cortex (TeA) of an adult mouse (Figure 1A-C). Here we present a conjugate “IF-SEM” dataset with co-registered immunofluorescence and electron microscopy, and a larger immunofluorescence-only “IF-only” dataset that does not include electron microscopy. The conjugate “IF-SEM” dataset is a subvolume of the “IF-only” dataset. We used 4 cycles of immunolabeling to localize synapses and quantify protein content (Table 1), choosing synapsin 1/2 as a general presynaptic marker and PSD-95 as a postsynaptic marker for glutamatergic synapses. Inhibitory synapses were distinguished by colocalization of GABA (presynaptic) and gephyrin (postsynaptic) (Figure 1D).

Postsynaptic receptors define the primary functional properties of glutamatergic synapses. AMPA-type receptors are tetramers of the subunits GluA1 – 4 in various combinations, while NMDA-type receptors are tetramers containing the obligatory subunit GluN1 together with GluN2A and GluN2B[57–60], in the mature neocortex. We therefore focused detection and analysis on these subunits (Suppl. Figure 1A), with the exception of GluN2A for which we were not able to identify a suitable antibody. After immunofluorescence imaging, we poststained sections with heavy metals and imaged a subregion of layer 2/3 using scanning electron microscopy (SEM) to reveal tissue ultrastructure. We then registered immunofluorescence channels with scanning electron micrographs from each section to generate volume multiplex images aligned with sub-micrometer precision. This powerful approach allows the identification of individual synapses by ultrastructure, and concomitant examination of scaffold and receptor molecules detected by immunofluorescence in those same synapses (Figure 1E-G).

Immunofluorescent labels for pre- and postsynaptic structures generally colocalized with those respective synaptic compartments in electron micrographs: synapsin and VGluT1 with presynaptic boutons, and PSD-95 and gephyrin with postsynaptic densities (Figure 1D). GABA colocalized with presynaptic boutons of inhibitory synapses, and (less brightly) with a subpopulation of postsynaptic dendrites and somata. Glutamate receptor subunits generally colocalized with PSD-95, but we also occasionally detected receptor immunolabeling outside of synapses. In some cases, extrasynaptic labeling was found in the spine apparatus, and in multivesicular bodies in dendrites (Suppl. Figure 1D), likely reflecting transport of receptors[61–63].

By following individual synapses across multiple sequential serial sections, we found robust staining for individual synaptic markers across sections within a single synapse (Figure 1E-G). This provides strong evidence for the specificity and sensitivity of immunolabeling at single synapses. The PSD-95 label was highly consistent, overlapping with ultrastructural postsynaptic densities in most glutamatergic synapses. In contrast, there was greater heterogeneity in receptor content for AMPA and NMDA receptor subunits (Figure 1E-G), even though transcriptomic surveys suggest that they are expressed by practically all neurons in mouse TeA (Suppl. Figure 2). We therefore set out to quantify this receptor content across the synapse population.

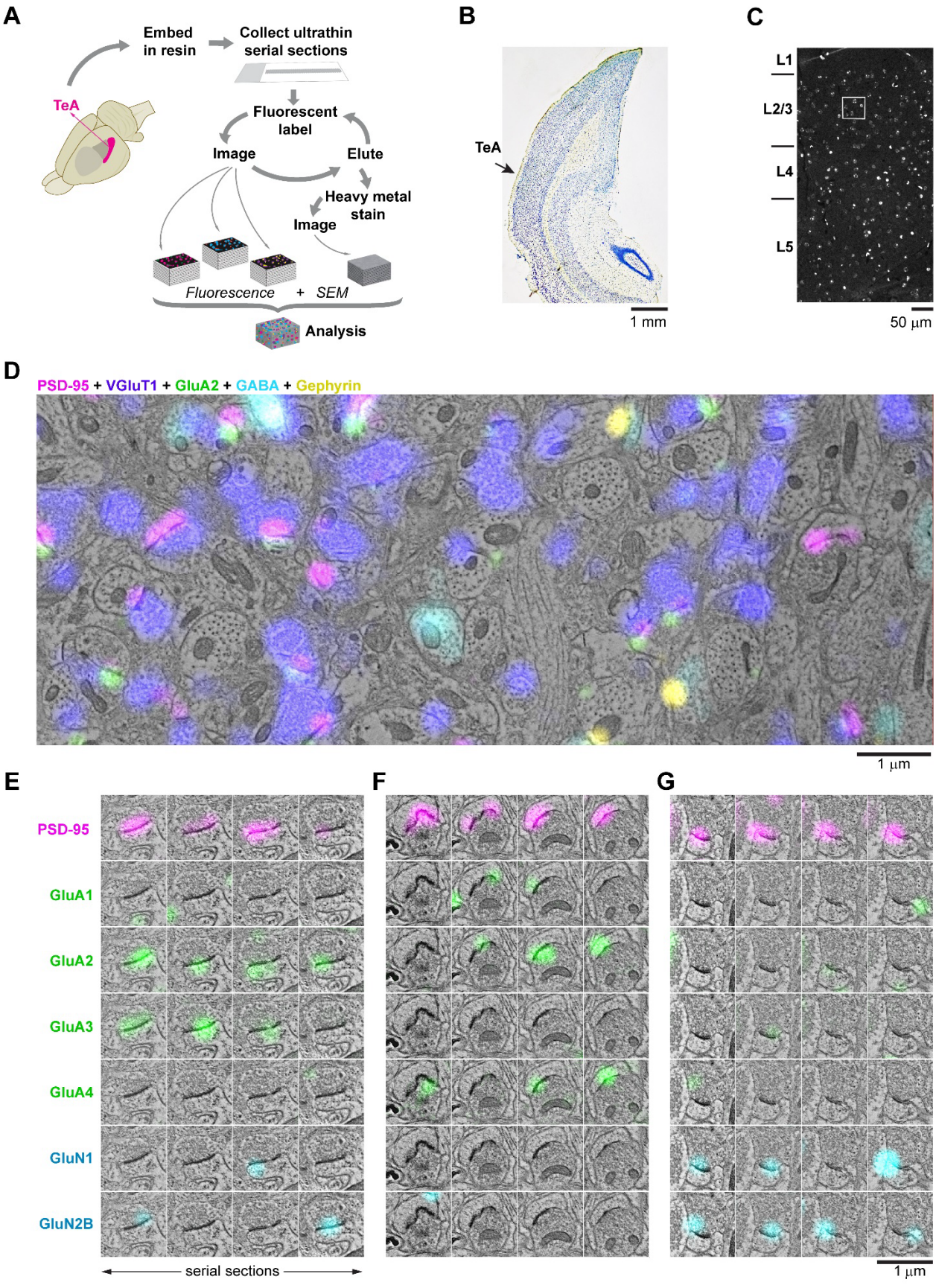

Figure 1. Conjugate array tomography enables multiplex immunolabeling of ultrastructurally-identified synapses
A. Array tomography method for serial sectioning, multi-channel IF and SEM imaging, and 3-D reconstruction of a block of layer 2/3 neocortex from the temporal association cortex (TeA) of adult mouse brain. **B**. Nissl stain of a section adjacent to the one

processed for array tomography, indicating the location of TeA. **C**. DAPI fluorescence from a 70 nm ultrathin section through TeA revealing cortical layers. Region of layer 2/3 chosen for reconstruction is boxed in white. **D**. Example of conjugate IF-SEM: overview of a larger area on one section with SEM and five IF channels (PSD-95 magenta, VGluT1 purple, GluA2 green, GABA cyan, and gephyrin yellow). **E-G**. Examples of synaptograms (IF +SEM) of 3 glutamatergic synapses with different combinations of AMPA and NMDA receptor subunits. For each synaptogram, rows represent different IF channels, and columns are serial sections through the synapse.

Proteometry of individual glutamatergic synapses reveals heterogeneity

We manually annotated 410 glutamatergic synapses based on visual inspection of electron microscopy images in the conjugate IF-SEM dataset (volume 12.1 x 12.1 x 2.6 μm^3; Figure 2A; see Methods) and subsequently quantified immunofluorescence for each channel associated with each synapse. This revealed consistent labeling of PSD-95 and glutamate receptor antibodies within annotated synapses (Figure 2A).

Analysis of the conjugate IF-SEM dataset showed that immunofluorescence measurements correlate well with ultrastructural data. Critically, we found a strong correlation (R^2 = 0.83) between synapse contact area (measured from SEM images) and summed PSD-95 content (measured from immunofluorescence images, Figure 2B). This provides a key validation, enabling future studies to estimate synapse size from immunofluorescence alone when using approaches such as expansion microscopy that do not support ultrastructural measurements with the same rigor as electron microscopy.

Motivated by the greater efficiency of immunofluorescence-only methods, which do not require labor-intensive electron microscopy imaging and analysis, we used the “ground truth” validation of synapses in our IF-SEM conjugate dataset to test the accuracy with which the molecular composition of synapses can be analyzed with immunofluorescence alone. To achieve unbiased automated detection of synapses in the IF-only dataset, we used a synapse detection tool developed specifically for array tomography[64] (Figure 2C; see Methods). This tool reliably detected annotated synapses in the conjugate dataset based on co-localization of synapsin and PSD-95 (Suppl. Figure 3). To minimize false positives, we set the probability threshold at 0.75, which resulted in 13% false positives and 23% false negatives, with detection failures biased towards the smallest synapses, and those with very low levels of PSD-95 immunoreactivity.

This synapse detection tool identified 4,767 glutamatergic synapses in the larger IF-only dataset (volume 46 x 44 x 3 μm^3). We used the synapse detection area as a mask to quantify immunofluorescence for each channel within individual synapses, and we excluded outliers with detection area > 2.5 μm^2 (Figure 2D, Suppl. Figure 4). The overall synapse size distribution and immunofluorescence measurements were comparable between the IF-only and conjugate dataset (Suppl. Figure 5).

Grouping synapses based on receptor content (average immunofluorescence intensity of for each synapse) by Ward clustering and silhouette analysis identified five distinct clusters (Figure 2E and Suppl. Figure 6). UMAP dimensionality reduction showed a compact grouping of clusters consistent with variations in size and expression of receptor subtypes (Figure 2F). Grayscale coding of UMAP projections by synapse size (summed PSD-95 immunofluorescence) or fluorescence intensity for individual channels revealed structured variation in molecular characteristics of single synapses (Figures 2G and S2).

The blue cluster contains large synapses with high levels of GluA2 and GluA3, and low levels of NMDA receptor subunits; while the green and purple clusters contain small synapses

with low levels of GluA2 and GluA3, and high levels of GluN2B subunits; and the red cluster contains high levels of GluA1 and GluA4 (Figure 2H). The orange cluster contains medium-size synapses with high levels of GluA2 but not GluA3, as well as smaller synapses with generally low levels of any receptors. The presence of a distinct cluster positive for GluN2B but negative for GluN1 (purple) is puzzling, since GluN1 is considered an obligatory subunit for NMDAR function[57,65]. This result may reflect the low average number of NMDA receptors per synapse[66–69], resulting in false negatives when immunolabeling for individual receptor subunits; indeed, for this reason many immuno-electron microscopy studies of NMDA receptor distribution at synapses have used cocktails of antibodies against several subunits[63,70]. It is possible, however, that this could also reveal a previously undescribed population of GluN1-negative NMDARs (that are presumably functionally-inactive), or separate trafficking routes for the two NMDAR subunits. Similar synapse groupings are evident in the conjugate dataset where synapses are manually annotated, precluding a potential artifact introduced by the automated synapse detection (Suppl. Figure 7).

Ward clustering of the receptors yielded three groupings, identical in both the IF-only and the conjugate AT datasets: GluA2 and GluA3, GluA1 and GluA4, and GluN1 and GluN2B (Figure 2E and Suppl. Figure 7). Thus, AMPA and NMDA receptors cluster separately, and short C-tail AMPAR subunits (GluA2 and A3) cluster separately from long C-tail subunits[71] (GluA1 and GluA4). Synapse clustering mirrors the three distinct biochemical and functional categories of receptor subunits. The overall consistency of the results using two different methods supports their validity and shows that immunofluorescence-only analysis is well suited to detect and quantify molecular properties of synapses.

Receptor content varies with synapse size

Visual inspection of synapses from the conjugate dataset revealed that many small synapses had low levels of immunofluorescence for AMPAR subunits and PSD-95 (Figure 3A) or were completely immunonegative for those channels (Figure 3A-C), but most of them were immunopositive for NMDAR subunits[12,70,72]. In comparison, larger synapses had strong PSD-95 immunolabeling in multiple sections overlapping with the ultrastructural postsynaptic density, and abundant expression of AMPAR subunits (usually GluA2 and GluA3), but much lower levels of NMDAR subunits (Figure 3D).

To quantify proteometry in relation to synapse size, we measured receptor subunit immunofluorescence (average intensity per voxel) across five logarithmically-scaled synapse size bins (Figure 3E). Immunofluorescence for PSD-95 and AMPARs increased with synapse size, while NMDAR immunofluorescence declined. Among AMPAR subunits, GluA2 and GluA3 showed the strongest dependence on synapse size[12,70,72]. Functional NMDARs in adult neocortex canonically contain GluN1 subunits together with GluN2A and/or GluN2B[73]; most NMDARs in the adult mouse cortex contain GluN2B[72,74–76].The observed decrease in GluN2B subunits at the smallest synapses might imply a potential preference for GluN2A at these synapses, although we lacked a suitable antibody to measure GluN2A.

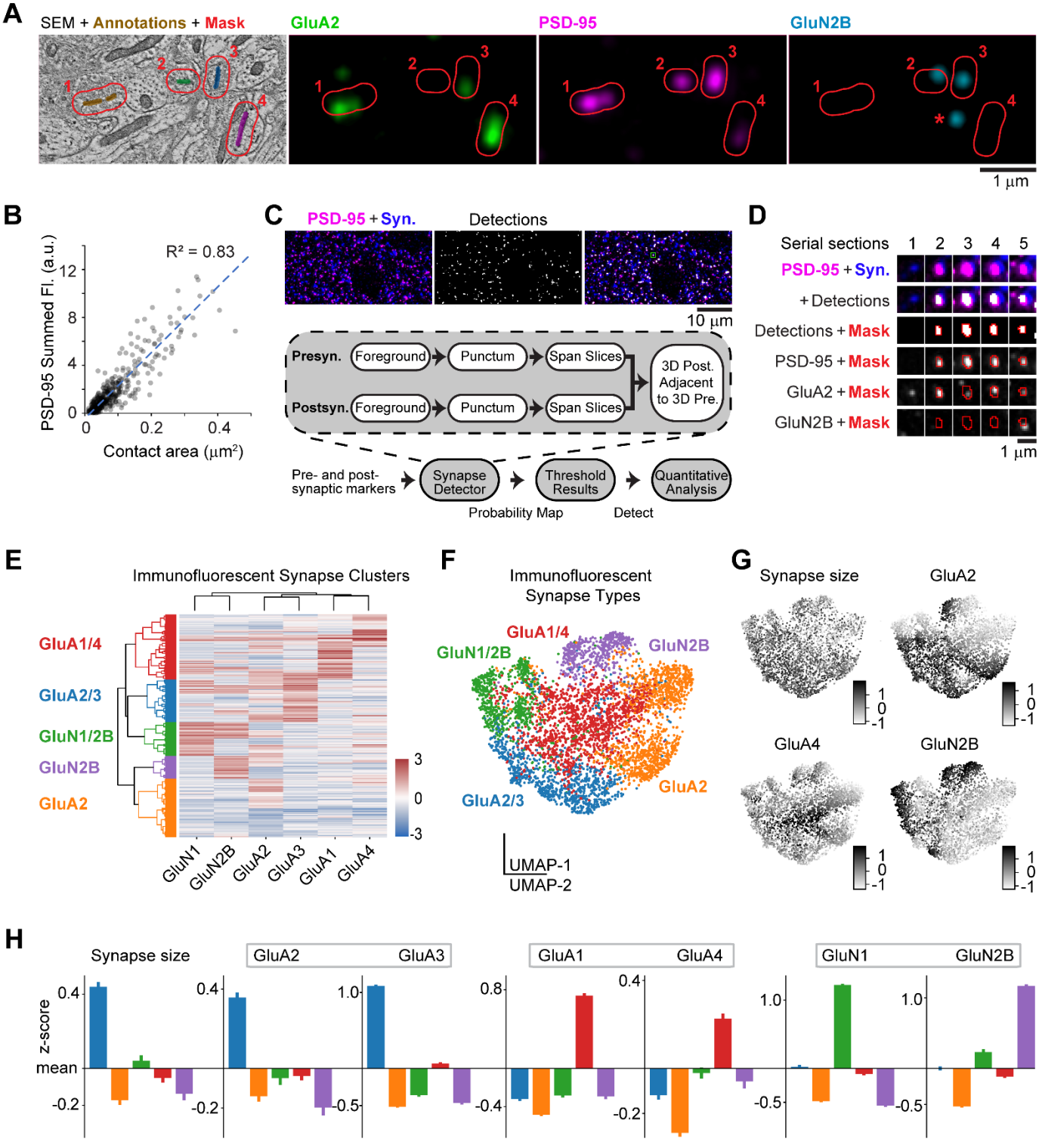

Figure 2. Proteometry of individual glutamatergic synapses reveals heterogeneity

A. Manual annotation of synapses from the IF-SEM dataset. Each synapse is assigned a different color. For every synapse, immunofluorescence intensities are measured within the masked area (in red), which expands the annotation by 160 nm (see Methods). In this section, synapses 1, 3, 4 are positive for GluA2; synapses 1-4 positive for PSD-95; and synapses 2, 3 positive for GluN2B. One GluN2B-positive punctum (asterisk) is not associated with a synapse. **B**. Scatterplot reveals a strong correlation between the synapse contact area and PSD-95 immunofluorescence as quantified in the conjugate dataset (n=410 synapses). **C**. Top, example of PSD-95 and synapsin immunofluorescence used for automated synapse detection and immunofluorescence measurements at synapses in the IF-only dataset. Below, method for automated detection of synapses from immunofluorescence data using probabilistic synapse detection. **D**. Synaptogram with detections and mask. **E**. Data-driven clustering groups glutamatergic synapses from the IF-only dataset into distinct clusters based on immunolabeling characteristics

(n=4,767 synapses). **F**. UMAP plot (colored by clusters defined in Panel E) shows clustering of distinct glutamatergic synapse subclasses in the IF-only dataset. **G**. Grayscale coding of UMAP projections by synapse size (summed PSD-95 immunofluorescence) and glutamatergic receptor expression in the IF-only dataset. **H**. Comparison of synaptic properties of each cluster; colors as in E and F.

Single-synapse analysis reveals covariance of receptor subunits

Multiplex immunolabeling allowed us to analyze how receptor subunits covary with one another and with changes in synapse size in the conjugate dataset (Figure 3 F-H and Suppl. Figure 8). We found strong positive covariance between the most common AMPAR subunits, GluA2 and GluA3, particularly in the largest synapses (upper right quadrant, Figure 3F). However, many GluA2-positive synapses were negative for GluA3 (lower right quadrant). In contrast, very few synapses were GluA2-negative and GluA3-positive (upper left quadrant), and all of these synapses were small. These results are consistent with biochemical evidence from hippocampus showing that GluA2 can exist in combination with different subunits, while GluA3 is almost exclusively found together with GluA2[77].

GluN1 and GluN2B, when present together, covaried positively and showed an inverse correlation with synapse size (upper right quadrant, Figure 3G), consistent with the size analysis in Figure 3E. A subset of synapses that were positive for GluN1 and negative for GluN2B also showed an inverse correlation with synapse size (lower right quadrant, Figure 3G). It is again surprising to find a group of synapses that are negative for GluN1 and positive for GluN2B, as in the purple cluster described above (upper left quadrant, Figure 3G).

To gain a deeper understanding of the AMPA and NMDA receptor content in relation to synapse size, we plotted GluA2 vs GluN2B. Three populations of synapses emerged, likely with distinct electrophysiological properties. The largest population comprised canonical synapses positive for both the primary AMPA (GluA2) and NMDA (GluN2B) receptor subtypes, in the upper right quadrant (Figure 3H). Within this population, larger synapses tended to have more GluA2 and less GluN2B, consistent with the general trends observed for AMPA and NMDA receptors. The lower right quadrant contained synapses positive for GluA2 and negative for GluN2B. Many synapses in this group were large, consistent with the positive correlation between AMPAR content and synapse size. These synapses may completely lack NMDARs, or may have GluN2A-containing receptors. A population of very small synapses that were positive for GluN2B but negative for GluA2 (top left quadrant, Figure 3H) represent putative silent synapses, likely present in the adult brain as well as during development[78]. Very few synapses were negative for both GluA2 and GluN2B, even though receptor content was not a criterion for synapse detection in our analysis (lower left quadrant, Figure 3H). We conclude that the presence of a postsynaptic density in adult neocortex implies functional ionotropic glutamate receptors even at the smallest synapses.

The postsynaptic target helps to predict synaptic composition

The ultrastructural information in the conjugate IF-SEM dataset allowed us to identify postsynaptic targets of individual synapses. Glutamatergic dendrites are spiny and GABA-immunonegative, whereas GABAergic dendrites are aspiny and GABA-immunopositive. Accordingly, to distinguish synapses onto glutamatergic dendritic shafts from those onto GABAergic dendritic shafts in our conjugate IF-SEM dataset, we first determined if the dendrites were GABA-immunopositive, and then followed the dendrites through the volume to determine if the dendrite itself was spiny.

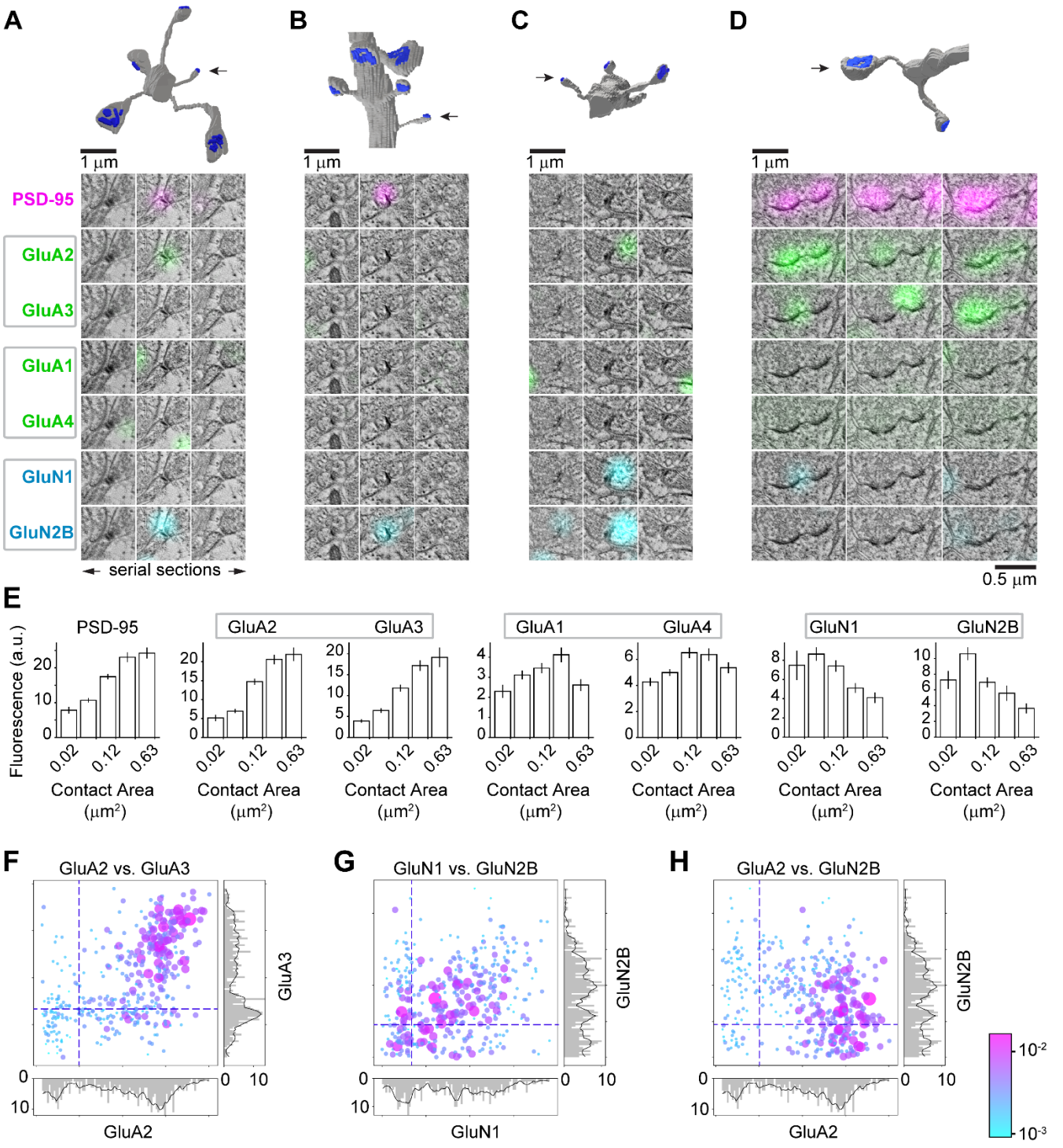

Figure 3. Small synapses are NMDAR-rich; large synapses are AMPAR-rich
A-C. Synaptograms of small synapses with a reconstruction of the parent dendrite on top. The synapse is indicated by an arrow; postsynaptic densities on spines are in blue. Fluorescence channels in this and subsequent figures are grouped following the data-driven clustering of glutamatergic receptor subunits shown in Figure 2E. **D**. Synaptogram of a large perforated synapse, showing much brighter immunolabeling for AMPARs and much weaker for NMDARs, compared to the small synapses in A-C. **E**. Histograms illustrate relationship of synapse composition to contact area in the conjugate IF-SEM dataset. X-axis histogram bins on log scale (n=410 synapses total; synapse counts per bin are n=41, n=158, n=134, n=63, and n=14 from smallest to largest contact area). **F-H**. Scatterplots comparing mean intensity across fluorescence channels at annotated synapses (conjugate IF-SEM dataset). Synapse contact area is encoded by the size and color of each dot. Dashed lines represent average fluorescence of each channel at GABAergic synapses from the same dataset, as an estimate of background.

Most synapses between glutamatergic neurons terminate onto spines, though a few terminate onto dendritic shafts. Glutamatergic synapses onto glutamatergic dendritic shafts were rare (12 out of 410 synapses, 2.9%) and tended to be small, with low levels of PSD-95 immunofluorescence (Figure 4A). Glutamatergic synapses onto GABA dendritic shafts were more common (50 out of 410 synapses, 12.2%) and comprised a distinct population exhibiting high levels of GluA1 and GluA4 immunofluorescence (Figure 4B). Synapses onto GABA-positive dendritic shafts were more densely packed along the dendrites than synapses onto non-GABA shafts (compare dendrite reconstructions in 4A and 4B), suggesting that these dendrites originated from parvalbumin interneurons[79,80].

We quantified the receptor content across three populations of glutamatergic synapses defined by their postsynaptic target. Synapses onto GABA dendrites contained reduced levels of PSD-95 (Figure 4C). Synapses onto GABA-negative dendritic shafts also contained less PSD-95 than synapses onto spines, although this did not reach statistical significance, due to the small number of shaft synapses. Interestingly, synapses onto GABA-negative shafts contained less GluA2 and GluA3, while synapses onto GABA-positive shafts had significantly more GluA1 and GluA4, compared to synapses onto dendritic spines (Figure 4C). AMPARs containing GluA1 and GluA4 without GluA2 exhibit fast kinetics and high calcium permeability[81], which position them to support high activity levels and suggest distinct plasticity mechanisms at excitatory synapses onto inhibitory interneurons[60,81,82].

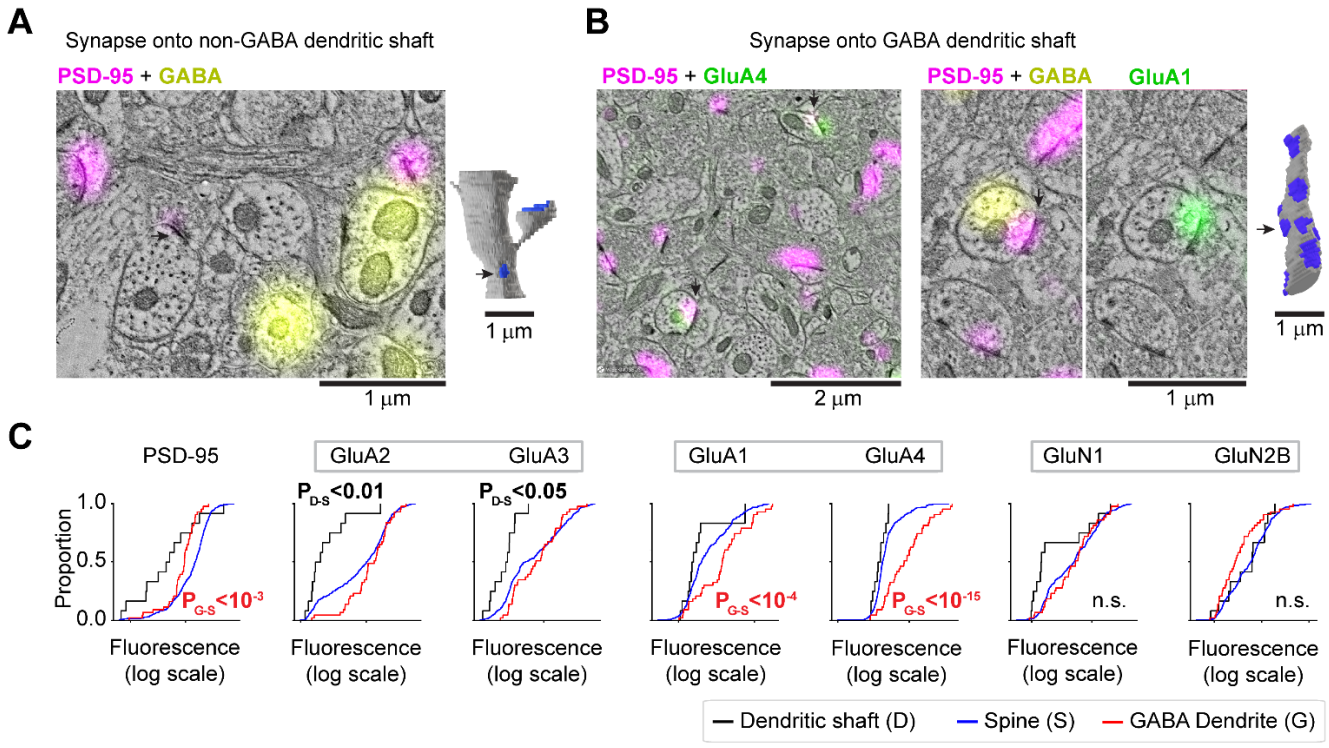

Figure 4. Receptor content of glutamatergic synapses depends on the postsynaptic target
A. Conjugate IF-SEM example of a glutamatergic synapse onto a GABA-negative dendritic shaft (reconstruction of parent dendrite on the right). These synapses tend to have weak PSD-95 fluorescence. **B**. Conjugate IF-SEM examples of synapses onto GABA-positive dendrites. The synapses on the left (arrows) are strongly immunopositive for GluA4; these synapses (higher magnification on the right) are also strongly immunopositive for GluA1. **C.** Cumulative frequency graph of receptor content of synapses, binned by postsynaptic target: synapses onto GABA dendrites have significantly more GluA1 and GluA4, and less PSD-95; synapses onto non-GABA (presumably glutamatergic neuron) dendritic shafts have significantly less GluA2 and GluA3. (n=352 spine-targeting, n=12 dendritic shaft-targeting, n=43 GABA dendrite-targeting synapses; Tukey-HSD test for all comparisons).

Immunofluorescence-only analysis at scale confirms heterogeneity of glutamatergic synapses

To test whether key features of synapse diversity can be detected using immunofluorescence array tomography, we repeated the analysis of receptor content in relation to synapse size using the larger IF-only dataset (Figure 5B). Here we used the summed PSD-95 immunofluorescence to estimate synapse size, based on the strong correlation between synapse contact area and PSD-95 immunofluorescence in the conjugate dataset analysis (Figure 2B). Results from the IF-only dataset were consistent with the conjugate dataset: GluA2 and GluA3 subunit content scaled with synapse size, while GluN1 and GluN2B content decreased.

Scatterplots of receptor co-variance were likewise consistent with the results from the conjugate dataset. GluA2 and GluA3 covaried at synapses where they are both present (upper right quadrant, Figure 5C); a population of synapses that was positive for GluA2 and negative for GluA3 was evident (lower right quadrant, Figure 5C); and a small group of synapses was negative for GluA2 and positive for GluA3 (upper left quadrant, Figure 5C). Plotting GluN1 against GluN2B (Figure 5D) showed the characteristic inverse dependence of NMDAR content on synapse size. This plot also revealed four groupings, one in each quadrant, with different combinations of GluN1 and GluN2B, consistent with the corresponding scatterplot from the conjugate dataset (Figure 3G). The plot of GluA2 against GluN2B revealed a grouping of synapses that were positive for GluA2 and for GluN2B in the upper right quadrant, and a grouping of synapses that were negative for GluA2 and positive for GluN2B in the upper left quadrant. In both of these populations, the synapses with high GluN2B content were small in size. The synapses that were positive for GluA2 but negative for GluN2B in the lower right quadrant were large, while the synapses that were negative for GluA2 and negative for GluN2B in the lower left corner were mostly small, consistent with the conjugate data analysis. Overall, the general patterns seen in the IF-only dataset agree with those in the conjugate dataset.

To assess information about the role of the postsynaptic target neuron in the IF-only dataset, we examined GABA immunofluorescence in the volume surrounding the synapse to identify putative synapses onto GABAergic interneurons. We first validated this metric using the conjugate IF-SEM dataset, finding that excitatory synapses in the vicinity of high GABA immunofluorescence were more likely than random synapses to terminate onto GABA targets. Indeed, when we selected the top 2% of synapses ranked by GABA immunofluorescence for ultrastructural examination, 88% of them were found to be onto GABAergic postsynaptic targets. This fraction decreased to 43% for the top 5%. In comparison, only 11.5% of all synapses in the conjugate dataset were onto GABAergic neurons.

This approach revealed that glutamatergic synapses adjacent to high GABA immunofluorescence (top 2%) had significantly more GluA1 and GluA4, but less PSD-95 than the remaining synapses, consistent with our results from the conjugate IF-SEM dataset (Figure 5F). We also found that synapses onto these likely GABA targets had significantly less GluA2[83] (Figure 5F). The difference in GluA2 content was not detected in the conjugate IF-SEM dataset (Figure 4C), likely due to the smaller sample size in that dataset. The IF-only approach therefore recapitulates many key results found with the conjugate dataset, but can be acquired more efficiently and for a much larger number of synapses. Importantly, our analysis of the conjugate IF-SEM dataset provides a key validation of the IF-only approach for future studies seeking to compare across multiple experimental conditions, or where equipment or expertise is not available for the more demanding conjugate IF-SEM approach.

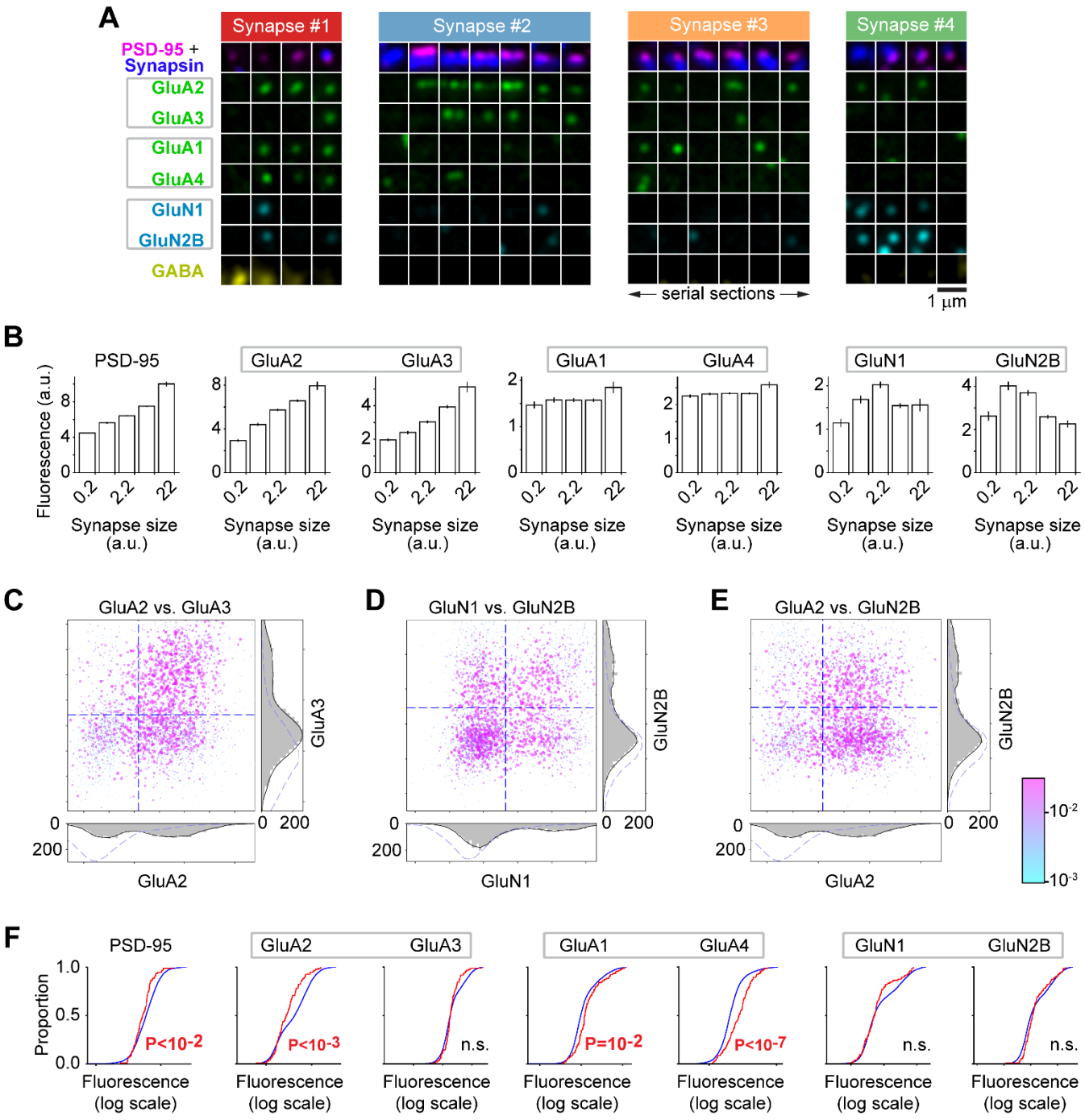

Figure 5. IF-only analysis at scale confirms key features of glutamatergic synapse heterogeneity
A. Synaptograms illustrate synapses of different sizes with different receptor composition. Synapses are color-coded at the top of each synaptogram by the corresponding synapse cluster as defined in Figure 2E, F. **B**. Histograms illustrate the relationship of synapse composition to synapse size (estimated by PSD-95 summed immunofluorescence). X-axis histogram bins on log scale (synapse counts per bin are n=583, n=1016, n=1646, n=1355, and n=134 from smallest to largest). **C-E**. Scatterplots comparing mean intensity across fluorescence channels at automatically detected synapses (IF-only dataset). Synapse detection volume is encoded by the size and color of each dot. Histograms show distribution of intensities for each axis (gray) and distribution of intensities in a shuffled set of synapse puncta locations from that channel (dashed), as an estimate of background. Dashed lines on the scatter plot represent the mean value + 1 standard deviation of the shuffled synapse puncta locations from the same dataset. **F**. For the IF-only dataset, fluorescence in a dilated GABA channel (mask is detection pixels dilated by 2 pixels) is used to identify synapses onto GABA targets. Cumulative frequency graph of receptor content of synapses onto putative GABAergic dendrites vs. the rest; like the conjugate dataset, synapses onto potential GABA targets (exhibiting the strongest 2% of GABA immunofluorescence) have significantly more GluA1, GluA4 and less PSD-95. Synapses with high GABA content also have significantly less GluA2. (n=96 high GABA content synapses; n=4626 low GABA content synapses).

NMDAR content of large glutamatergic synapses is related to spine neck diameter

The large number of synapses detected in our IF-only dataset uncovered an uncommon feature of glutamate receptors distribution: while NMDAR content overall is inversely correlated with synapse size (Figure 3E, Figure 5B), a subpopulation of medium and large synapses have high GluN1 and/or GluN2B immunofluorescence (Figure 5D). Deeper inspection of this population suggests that these synapses also contain high levels of GluA2 (Figure 5E). This caught our attention, because high levels of NMDAR likely endow these synapses with distinct functional properties.

To examine the ultrastructure of these synapses, we leveraged the conjugate dataset where this population is also present, but less noticeable due to the smaller number of synapses (Figure 3G,H). To our surprise, many NMDAR-rich spines had a distinctive morphology, with exceptionally wide spine necks (Figure 6A).

The diameter of the spine neck may influence its function[84–88], and the conjugate dataset allows systematic analysis of the relationship between spine neck, synapse size, and receptor content. As previously reported, spine head diameter correlated closely with synapse contact area[8] (Figure 6B). However, we found that spine head diameter was independent of spine neck diameter (Figure 6C). We therefore partitioned large spines (head diameter ≥ 250 nm) into those with thin necks (diameter < 180 nm) and thick necks (≥180 nm). The average head diameter of these two spine populations was similar (Figure 6D), but as expected the thick-necked spines had a significantly lower ratio of head to neck diameter (Figure 6E).

Plotting GluN2B immunofluorescence against neck diameter revealed a positive correlation between neck diameter and NMDA receptor content (Figure 6F), while GluN2B showed a weak negative correlation to synapse size (Figure 6G), consistent with our synapse size analyses (Figure 3E, Figure 5B). Separate analysis of the synapses onto thin-necked versus thick-necked dendritic spines confirmed that thick-necked spines have higher GluN2B content (Figure 6H), and higher levels of GluA1, suggesting a potential for greater plasticity of these synapses[73].

Receptor content correlates more strongly with synapse ultrastructure than with parent neuron identity

The molecular composition of synapses is determined, at least in part, by the identity of the parent neurons. Consistent with this, we detected differences between the receptor content of synapses onto glutamatergic vs. GABAergic dendrites (Figure 4). To further explore the influence of parent neurons, we identified synapses within the conjugate dataset that share the same postsynaptic dendrite (Figure 7A), the same presynaptic axon, or both. As expected, pairs of synapses onto a glutamatergic and a GABAergic dendrite (GABA-Glut Mix, Figure 7C,D), had higher divergence in receptor content than the population of all synapse pairs. Conversely, pairs of synapses sharing the same postsynaptic dendrite (n=412 pairs) were more similar in receptor content than all synapse pairs, however, the magnitude of this effect was surprisingly modest. We also identified a small number of synapses sharing the same presynaptic axon (n=70 pairs), but for this limited sample we found no significant differences in similarity compared to all synapses. To permit a more extensive visual examination of these results, we color-coded subsets of synapses based on parent dendrite identity within the UMAP projections (Figure 7B), but failed to find any clear evidence that synapses that shared the same postsynaptic dendrite grouped together.

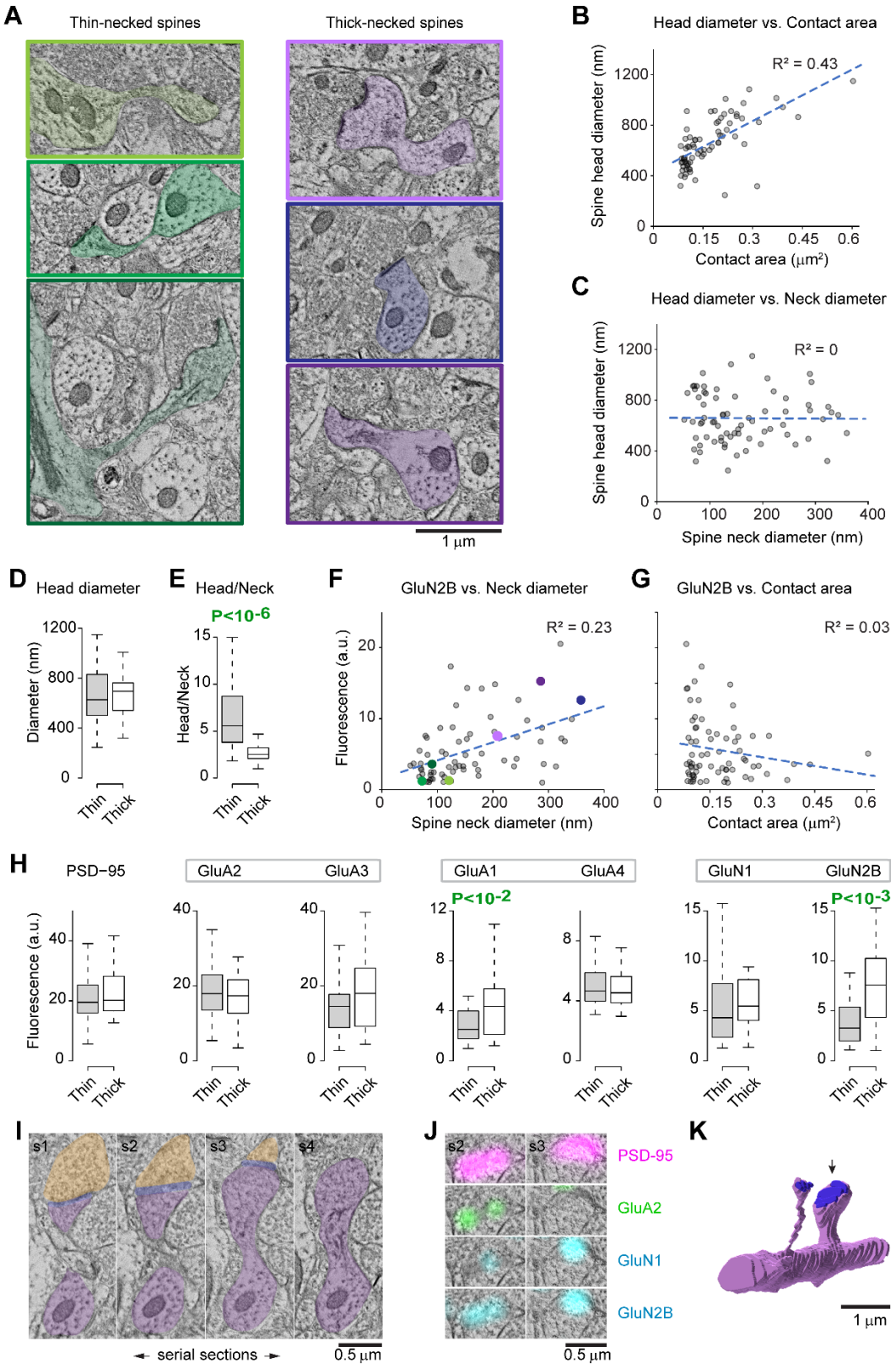

Figure 6. Receptor content of large glutamatergic synapses correlates with spine shape

A. Examples of large spines with thin necks (<180 nm diameter) vs. those with thick necks (≥180 nm diameter), with the color corresponding to the color dots in F. **B, C**. Scatterplots show that the spine head diameter has a strong positive correlation with synapse size (B), but no correlation with neck diameter (C). Only large spines (head diameter ≥ 250 nm) are included in these scatterplots, n= 72. **D, E**. Thin- and thick-necked spines have similar head diameters (D), but a significantly different ratio of head/neck diameters (E) based on a sample of 50 thin-necked spines and 22 thick-necked spines. Statistical significance (t-test) is indicated on the plot. **F**. Scatterplot shows a positive correlation between GluN2B average fluorescence and spine neck

diameter of large spines. GluN2B and spine neck size are positively correlated. The colored dots correspond to the spines in C with the same color box. N=72 large spines. **G**. Scatterplot of GluN2B average fluorescence vs. contact area, showing weak negative correlation. **H**. Comparison of receptor content of thin-necked vs. thick–necked spines. Statistical significance (t-test) is indicated on the plot. Synapses onto spines with thick necks have significantly more GluA1 and GluN2B immunofluorescence. **I**. Four serial sections through a thick-necked spine. The spine is segmented out in purple, the presynaptic bouton in yellow, and the postsynaptic density in blue. **J**. Immunofluorescence for PSD-95, GluA2, GluN1 and GluN2B in two of the sections through the synapse. **K**. Volume reconstruction of the same thick-necked spine, indicated with an arrow.

Prompted by the correlation between receptor content, synapse size and spine neck size (Figure 6), we next defined three populations of axospinous synapses based on distinctive morphology: “classical” spines with well-defined spine head and spine apparatus, including a perforated postsynaptic density and presence of presynaptic mitochondria (n=33); thick-necked spines, with a neck diameter ≥ 180 nm and head diameter ≥ 250 nm (n=22); and small spines with a head diameter < 250 nm (n=23). There was partial overlap within the first two categories (8 spines) (Figure 7E,F).

Notably, we found that synapses onto ultrastructurally-defined spine types clustered together on the UMAP projection (Figure 7F) and exhibited greater similarity in receptor content than synapses sharing pre- or postsynaptic parent neurons. Synapses onto classical and thick-necked spines clustered together with other large synapses with high AMPAR content, but the two populations showed some separation (Figure 7F,G). Synapses onto small spines clustered separately with other small NMDAR-rich synapses. Synapses belonging to each of these ultrastructurally-defined spine types were more significantly similar to one another than to the population of all synapses.

We therefore conclude that parent neuron identities have relatively little influence, and that spine morphology is a far better predictor of glutamatergic receptor content at axospinous synapses. The strong similarity of synapses onto classical spines likely reflects stability of these synapses[89–91] and an optimization of receptor content for their primary role in robust transmission of information. This important result is consistent with a key role for synapse subclasses as distinct computational units that are not simply defined by parent neurons[92].

Discussion

Besides serving as key nodes of communication between neurons, synapses also act as independent computational units. Insight into the functional specialization of synapses in the mammalian brain is constrained by the techniques available to quantify their molecular diversity. These techniques must contend with the small size and high density of synapses within the brain. Consequently, far less is known about their heterogeneity and specialization than larger-scale circuit components such as cell types and microcircuits.

Here we leverage the unique capacity of conjugate array tomography to probe the chemical architecture of synapses within the ultrastructural context of the brain. Using machine-learning classification approaches, we find that glutamatergic synapses in the neocortex group into distinct clusters based on their content of receptor subunits. Previous studies have clustered synapses based on non-receptor proteins in dissociated hippocampal cultures[93–95], or on optically-measured colocalization of two postsynaptic scaffolding proteins[29,96]. Proteomic analyses of bulk synaptosome preparations reveal co-regulation of groups of proteins that may correlate with synapse subclasses[32] and molecular specialization of synapses from genetically defined synapse types[97]. However, no such proteometric clustering has previously been reported in the intact brain.

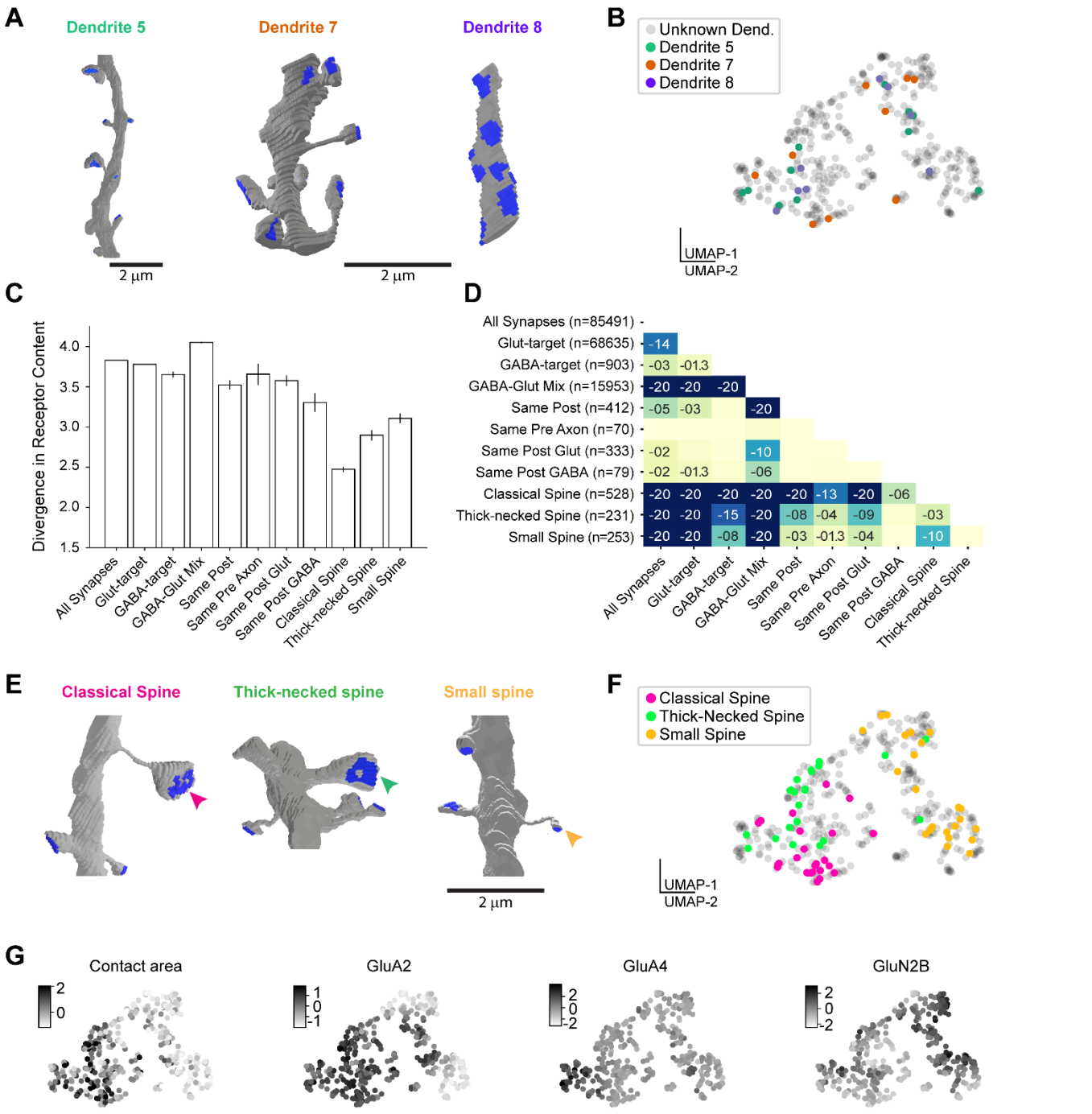

Figure 7. Receptor content of synapses is only partially determined by the pre- and postsynaptic neuron
A. Example of synapses onto the same dendrite, with postsynaptic densities in blue. Dendrite #8 is GABAergic. **B**. UMAP plot with synapses targeting the same dendrite identified by the same color. Synapses onto the same postsynaptic target show only weak evidence of clustering. **C**. Analysis of the divergence in receptor content of synapses, depending on the postsynaptic target, presynaptic axon, and spine morphology. Synapses sharing the same postsynaptic dendrite are more similar in receptor content compared to all synapses, but the difference is very small. In comparison, synapses onto morphologically-defined spine types show much higher similarity. (All synapses n=85,491 pairs; glutamate-targeting n=68,635 pairs; GABA-targeting n=903 pairs; GABA- and Glut-targeting mix=15,953 pairs; same postsynaptic dendrite n=412 pairs; same presynaptic axon n=70 pairs; same postsynaptic glutamate-targeting n=333 pairs; same postsynaptic GABA-targeting n=79 pairs; classical spine n=528 pairs; thick-necked spine n=231 pairs; small spine n=253 pairs) **D**. Table with all the statistics for C, numbers represent the exponent of the probability as estimated by Tukey HSD test. **E**. Examples of morphological groups of dendritic spines: “Classical” spines contain a spine apparatus postsynaptically, a mitochondrion presynaptically, and a perforated postsynaptic density. Thick-necked spines are spines with a neck diameter ≥ 180 nm. Small spines are defined as spines with a head diameter < 250 nm. **F**. UMAP plot showing clustering of synapses onto the three different morphological groups of spines. **G**. Grayscale coding of UMAP projections by synapse size (contact area) and glutamatergic receptor expression in the conjugate IF-SEM dataset.

Our focus on synaptic receptors permits functionally-relevant insight into the logic underlying the specialization of glutamatergic synapses. By registering volume electron microscopy with immunofluorescence, we demonstrate that specific proteomic features are associated with distinct ultrastructural characteristics, and we identify a distinct group of NMDA-rich synapses onto large thick-necked spines. Synapse diversity has been correlated with the identity of the pre- or post-synaptic parent neuron[8,98–100], but we find that the identity of the parent neurons accounts for only a modest fraction of the molecular and ultrastructural diversity of synapses, suggesting that synapse subclass itself may be a fundamental element of neuronal circuit structure[92].

Limitations of the current study

Our data were from the TeA cytoarchitectonic field of a 16-month old mouse (roughly corresponding to a 50 year-old human). By avoiding interanimal variability, deep analysis of a single animal limits technical measurement noise, as in previous labor-intensive connectomic datasets[101,102]. TeA is homologous to human temporal association cortex, facilitating comparison with neurosurgically resected tissue blocks (whose tissue quality is far superior to post-mortem samples)[103–107], since these blocks are typically resected from the middle temporal gyrus to access an underlying epileptic focus[103]. The manual annotation of synapses in the electron microscopy images limited the size of the conjugate array tomography dataset compared to the more efficient, automated synapse detection used for immunofluorescence-only analysis, but allowed rigorous validation of the larger dataset.

We used a carefully selected and validated set of commercial antibodies to assess the distribution of receptor subunits in a reproducible manner[10,108–110]. However, the performance of the antibodies was variable. The GluA1 signal showed less sensitivity and higher background than the other antibodies, but we retained GluA1 in our dataset based on its colocalization with PSD-95, and robust labeling of select individual synapses (e.g. Figure 1F and 5A). We detected a cluster of synapses immunopositive for GluN2B but immunonegative for GluN1, even though GluN1 is an obligatory subunit for functional NMDA receptors[57]. This observation must be treated cautiously because it could arise from stochastic noise, reflecting limited labeling efficiency and the fact that there are fewer copies of NMDA receptors per synapse compared to AMPA receptors[66–69]. However, the observation might suggest a previously undescribed population of functionally inactive GluN1-negative NMDARs, or separate trafficking routes for the two subunits.

Our automated synapse detector enabled efficient analysis of synaptic populations using immunofluorescence only. This approach is more accessible and scalable than conjugate IF-SEM array tomography. Furthermore, the validity of the IF-only approach was largely supported by direct comparison of the immunofluorescence and electron microscopic detection of synapses. However, automated synapse detection based on immunofluorescence failed to reliably identify the smallest synapses which span only one or two sections and have low levels of immunoreactivity for synaptic markers.

Factors predicting receptor expression

We found that glutamatergic synapses in TeA cortex group into subclasses based on glutamate receptor content, implying distinct physiological roles. For example, the blue cluster of large synapses with high expression of GluA2/GluA3 and low expression NMDAR subunits represents strong synapses, while the purple and green clusters of small synapses low in

AMPARs and high in NMDARs likely include weak or silent synapses. The functional specialization of synapses is further highlighted by the clustering of glutamate receptor subunits at synapses according to the distinct biochemical and functional categories of these subunits; AMPA and NMDA receptors clustered separately, and short C-tail AMPAR subunits (GluA2 and A3) clustered separately from long C-tail subunits[71] (GluA1 and GluA4).

Many factors contribute to the diversity of glutamatergic synapses, including the phenotype of the pre- and postsynaptic neurons, the regional neurochemical milieu of the synapse, and the history of neural activity. Our data confirm that the postsynaptic target is an important predictor of the receptor content of excitatory synapses. For example, we found markedly lower levels of PSD-95, GluA2, and GluA3 at glutamatergic synapses onto excitatory dendritic shafts, compared to those onto dendritic spines. We also detected differences in the receptor composition of synapses onto GABAergic dendrites relative to those onto glutamatergic dendrites. Although our data did not allow clear identification of different subclasses of GABAergic interneurons, synapses onto GABAergic dendritic shafts expressed high levels of GluA1 and GluA4. Based on the fast kinetics and high calcium permeability of these receptor subtypes[81], this receptor specialization is consistent with suggestions that inhibitory neurons may play a special role in high-frequency signaling.

Extending this approach to analyze more synapses in a larger neocortical dataset through array tomography or multiplex expansion microscopy[95,111–114] would likely reveal additional uncommon clusters and would also allow clear identification of subgroups within the clusters reported here. Likewise, extending this analysis to detection of additional synaptic proteins and features, and to examination of additional brain structures, species, and stages of neurodevelopment or aging would likely uncover new discrete clusters of synapse subclasses, as well as continuous sources of variation within existing subclasses. In this respect, our work provides key validation for the use of immunofluorescence for synapse analysis. For example, synaptic contact area is an important surrogate for unitary transmission strength[1,2,4,115] but cannot be measured directly using traditional light microscopy. Our results establish a means of estimating this variable from immunofluorescence data: we demonstrate that synaptic contact area based on volume electron microscopy (the gold standard) correlates strongly with PSD-95 immunofluorescence. This supports synapse size estimation with other super-resolution immunofluorescence modalities, such as expansion microscopy, that are incompatible with electron microscopy[54,93,111,116].

Spine morphology and receptor content

Synapses onto large “classical” mushroom-shaped spines contained high levels of AMPARs and few NMDARs, whereas those onto small spines contained relatively fewer AMPARs and more NMDARs, consistent with previous reports[12,70,72]. Notably, we also found that large spines with thick necks comprised a distinct group associated with both high AMPAR and high NMDAR content. The existence of specialized thick-necked spines has been suspected based on the skewed distribution of neck sizes[117], but there was no previous evidence that such spines have a distinct molecular composition.

Spines with thick necks permit rapid diffusion of calcium and other signaling molecules into the dendrite[85,86], where they could engage signaling pathways not localized to the spine, allowing thick-necked spines to exert more influence over the parent dendrite. This is consistent with their high levels of NMDAR channels, whose slow kinetics and high calcium permeability play a special role in synaptic plasticity, and probably also in learning and memory. Conversely, a thicker neck would also support greater diffusion from the parent dendrite into the spine,

making them more sensitive to cell- and dendrite-wide signaling and allowing more rapid changes to the chemical composition of the synapse[85,86,118]. Restricted spine neck size may also reduce electrical conductance, providing electrical isolation for thin-necked but not thick-necked spines[87,88], although this idea remains controversial due to difficulty of measuring spine voltage[85,86,118,119].

Histological identification of putative silent synapses

We identified a subgroup of small synapses that contained NMDARs but no detectible AMPARs. These synapses likely correspond to electrophysiologically-defined postsynaptically-"silent" synapses, which have been posited as a key players in long-term potentiation[120–122]. Because immunocytochemistry detects protein directly, our study gives independent orthogonal support for the reality of "silent" synapses. It remains possible that some of these synapses may actually express AMPARs, albeit at level below the threshold for antibody detection; whether so few AMPARs would be sufficient to remove the voltage-dependent block of NMDARs is debatable. While previous work described synapses lacking NMDARs in juvenile rodents[12,70,72], our study supports the notion that silent synapses persist through adulthood and are thus likely to continue to be involved in circuit remodeling, building on a recent study of younger adults[78].

Synapse subclasses as computational units

We found that AMPA and NMDA receptor content of axospinous synapses were only weakly predicted by pre- or postsynaptic parent neuron identity. This is surprising. The molecular composition of a synapse is surely constrained by the pre- and postsynaptic neurons' transcriptomes, and synapses that share the same parent neurons tend to be more similar in size than random synapses[98,100]. However, we find that ultrastructural features are much stronger predictors of glutamate receptor content. For example, synapses onto anatomically defined "classical" spines with a large mushroom head showed much greater molecular similarity to other synapses onto other classical spines than to synapses sharing the same pre- or post-synaptic parent neuron (Figure 7). These results are consistent with a key role for synapse subclasses as distinct computational units that are not simply defined by parent neurons[92].

Implications for future research

The molecular composition of synapses changes dramatically during postnatal development. Synapses are especially modifiable before maturity, but remain highly plastic even in the adult mammal. Multiple factors, including the tissue environment and the location on the postsynaptic neuron, can influence the morphology and composition of synapses. The precise history of activity at each synapse and the resulting pattern of exposure to diffusible neuromodulators can likewise drive synaptic variability. However, as sites of memory storage, synapses must also possess a capacity for "stability". Physiological literature has implicated transitions between discrete states as a primary basis for glutamatergic synaptic plasticity[20,21,123–129], and theoretical studies propose discrete states with barriers to transition as a basis for synaptic stability[124,130–133]. This raises the possibility that our subclasses from a single proteometric snapshot may represent samples from a dynamic population, where activity-dependent plasticity is driving transitions by individual synapses over energy barriers separating discrete stable states. New avenues for imaging glutamate receptors in behaving animals will be instrumental in addressing these questions[134].

Recent technical improvements are driving rapid advances in connectomics based on structurally identified connections with volume electron microscopy[101,102,135–140]. However, the functional impact of connections between two neurons or brain structures depends on the strength and physiological features of each synapse in that connectome. Improved methods for qualitative and quantitative estimation of these features from ultrastructural evidence will be essential for future generations of connectomics. Ultrastructural correlates that distinguish excitatory from inhibitory synapses were identified 50 years ago[141–143], while more recent work has begun to elucidate the relationship between synapse size and synaptic strength[1,2,4,115] or even ultrastructure and neurotransmitter content[144]. Conversely, new methods in expansion microscopy and multiplex super-resolution imaging can provide increasingly rich molecular information about single synapses[93,99,111–114], although at the expense of ultrastructural context (but see[145–147]). Our direct measurement of receptor content rigorously aligned with ultrastructural features at single-synapse resolution represents an important step toward a functional interpretation of connectomes.

Animal models and genetic studies of debilitating neuropsychiatric disorders, including obsessive-compulsive disorder, autism, and schizophrenia, point to synaptic proteins as a critical locus of the underlying circuit dysfunction [35–40,148]. While numerous studies focus on identifying the cell type or brain region that underlies these disorders, our results suggest that synapse subclass may be an important but overlooked organizational principle for the etiologic mechanisms and treatment of these disoredrs[94]. Advances in array tomography, expansion microscopy, super-resolution imaging, and quantitative proteomics are ideally positioned to offer new insights.

Acknowledgments. We thank Forrest Collman, Uygar Sümbül, Michael Hawrylycz and members of the Owen lab for helpful comments. We also wish to thank Allen Institute founder, the late Paul G. Allen, for his vision, encouragement, and generous support.

Funding: This work is supported by funding from a Brain and Behavior Research Foundation Young Investigator Award (to SFO), the Stanford Maternal and Child Health Research Institute (to SFO), the Shurl and Kay Curci Foundation (to SFO), the Foundation for OCD Research (FFOR), the John A. Blume Foundation (to SFO), NS039444 (to RJW), and an NIH Director's Office Transformative Research Award, R01NS092474 (to SJS).

Author Contributions: Conceptualization: KDM, SJS, RJW; Methodology: KDM, AKS, JS, SJS, RDW, SFO; Software: AKS, SFO; Validation: KDM, AKS, JS, SFO; Formal Analysis: KDM, AKS, JS, SJS, RJW, SFO; Investigation: KDM, AKS, JS, SJS, RJW, SFO; Resources: SJS, RJW, SFO; Data Curation: KDM, AKS, JS, SJS, RJW, SFO; Writing: KDM, SJS, RJW, SFO; Supervision: KDM, SJS, RJW, SFO; Funding Acquisition: KDM, SJS, RJW, SFO.

Declaration of Interests: K.D.M. and S.J.S. have founder's equity interests in Aratome, LLC (Menlo Park, CA), an enterprise that licenses high-multiplex immunostaining materials, and are also listed as inventors on two United States patents on array tomography methods that have been issued to Stanford University (United States patents 7,767,414 and 9,008,378). All other authors declare no competing interests.

Methods

Specimen preparation and array tomography methods closely parallel those previously described in detail[10,41,42,64,109]. Those details are summarized briefly here, alongside new particulars where needed.

Animals. Adult C57BL/6J mice were used for this study. The conjugate volume and the larger, IF-only volume, are from a 16-month old male mouse (M4926). All animal procedures were performed in accordance with the University of North Carolina animal use committee's regulations.

Mice were deeply anesthetized with pentobarbital/ketamine; after a brief saline flush, they were perfusion-fixed with a mixture of 2% glutaraldehyde/2% formaldehyde, in 0.1M cacodylate buffer, pH 7.0, with the addition of 2 mM $CaCl_2$ and 2 mM $MgSO_4$. The brain was removed and postfixed overnight at 4°C in the same fixative. 50 μm-thick sections were cut on a Vibratome and collected in 0.1 M phosphate buffered saline. Relevant sections were cryoprotected in 30% glycerol and quick-frozen onto an aluminium block cooled on dry ice, to aid in reagent penetration. Cold sections were quickly placed into vials containing ethanol + 0.1% uranyl acetate at -70° in a Leica AFS machine. After 24 hours dehydration, ethanol was progressively replaced with HM-20 Lowicryl resin at -50°C. After plastic infiltration was complete, sections were sandwiched between sheets of ACLAR polychloro-trifluroethylene plastic, and exposed to long-wavelength UV light as incubation temperature was gradually increased over 18 h to room temperature. The ACLAR was peeled off the polymerized wafers and small blocks containing TeA auditory association cortex were cut out of the sections and glued to polymerized cylinders of epoxy plastic. The blocks were mailed to Stanford University for subsequent thin sectioning, immunolabeling and fluorescence imaging.

Substrate coating. Schott Nexterion A+ coverslips (Fisher Scientific) were used as a substrate for collection. The functionalized aminosilane glass was carbon coated using a Cressington 308R Coater to ensure strong adhesion of the section ribbon to withstand subsequent harsh treatments, and to improve conductivity for the scanning electron microscope. Coverslips were coated three times for 9.9 seconds each, resulting in a total deposit of ~ 3nm of carbon on the surface.

Ultrathin sectioning. The blocks were trimmed around the tissue to the shape of a trapezoid approximately 1.5 mm wide and 0.5 mm high, and glue (Weldwood Contact Cement diluted with xylene) was applied with a thin paint brush to the leading and trailing edges of the block pyramid. Ribbons of 70-nm-thick serial sections were cut on an ultramicrotome (Leica Ultracut EM UC6) and mounted onto carbon-coated aminosilane coverslips prepared as described above. After the sections dried, they were kept on a slide warmer set at 55°C for 30 minutes, and then stored until immunolabeling within 1 week from sectioning.

Immunofluorescence labeling. The sections mounted on the coverslips were immunolabeled as previously described[10]. Sections were pretreated with freshly made sodium borohydride [1% in Tris-buffered saline (TBS), pH 7.6 for 3 min] to reduce non-specific staining and autofluorescence. After a 20 min wash with TBS, the sections were incubated in 50 mM glycine in TBS for 5 min, followed by blocking solution (0.05% Tween 20 and 0.1% BSA in TBS) for 5 min. The primary antibodies (listed in Table 1) were diluted in blocking solution and applied overnight at 4°C. After a 15-min wash in TBS, the sections were incubated with highly cross-adsorbed Alexa Fluor conjugated secondary antibodies (ThermoFisher Scientific), diluted 1:150 in blocking solution for 30 min at room temperature. Finally, sections were washed with TBS for 15 min, rinsed with distilled water, and mounted on glass slides using SlowFade Diamond Antifade Mountant with DAPI (ThermoFisher Scientific S36964). After sections were imaged, the

antibodies were eluted using a solution of 0.2 M NaOH and 0.02% SDS for 20 minutes, and new antibodies were reapplied, as needed. All staining rounds included the DAPI label to facilitate image registration between rounds.

Antibodies. All antibodies were from commercial sources and have been extensively validated for AT in previous studies[10,41,109,110,149,150].

Table 1: Antibodies used for Dataset 201228 (12 antibodies, 74 serial sections, 70 nm each)

Antibody	Source	RRID	Dilution	2º Ab (nm)
Cycle 1				
GluN1	mouse, SySy 114 011	AB_887750	1:500	594
GluA1	rabbit, Millipore #AB1504	AB_2113602	1:100	488
VGluT1	guinea pig, Millipore AB5905	AB_2301751	1:5000	647
Cycle 2				
GluA3	mouse, Millipore MAB5416	AB_2113897	1:1000	594
GluA2	rabbit, Abcam ab206293	AB_2800401	1:50	488
Synapsin 1/2	chicken, SySy 106 006	AB_2622240	1:100	647
Cycle 3				
GluN2B	mouse, NeuroMab N59/36	AB_2232584	1:500	594
GluA4	rabbit, Cell Signaling 8070	AB_10829469	1:50	488
MBP	chicken, AVES MBP	AB_2313550	1:100	647
Cycle 4				
Gephyrin	mouse, NeuroMab L106/93	AB_2636852	1:100	594
PSD-95	rabbit, Cell Signaling 3450	AB_2292883	1:100	488
GABA	guinea pig, Millipore AB175	AB_2278931	1:5000	647

Fluorescence imaging and image processing. The immunostained ribbon of sections was imaged on an automated epifluorescence microscope (Zeiss AxioImager Z1) using a 63x Plan-Apochromat 1.4 NA oil objective. To define the position list for automated imaging, a custom Python-based graphical user interface, MosaicPlanner (Dr. Forrest Collman[151], obtained from https://code.google.com/archive/p/smithlabsoftware/), was used to find corresponding locations across the serial sections. An area of 46 x 44 μm in layers 2/3 was selected for analysis. The images were registered between staining cycles and aligned based on the DAPI signal, using the MultiStackReg plugin in FIJI[152]. Background was subtracted using the Subtract Background function in FIJI, with a rolling ball radius of 50. Images were normalized with the Enhance Contrast function in Fiji by setting saturated pixels value at 0.01%. Occasional brightly fluorescent specks of contamination were masked out to not interfere with the normalization. This volume is referred to as IF-only volume in the Results section.

Post-staining. Following 4 rounds of multiplex fluorescence imaging, the ribbons were rinsed with water, dried and mailed to the Allen Institute for SEM imaging. To increase contrast, the sections were first poststained for 1 min with a freshly-made solution of 0.1% $KMnO_4$

dissolved in 0.1N H_2SO_4, followed by 5% aqueous uranyl acetate for 30 min, rinsed in water, and then 1% Reynolds' lead citrate, freshly prepared and filtered, for 1 min[41]. Sections were then rinsed in water and air dried.

SEM imaging. A Zeiss Gemini 500 using Atlas V software was used to acquire the correlative EM dataset. A 4x4 mosaic with a size of 49.2 μm x 49.2 μm in layer 2/3 was acquired for each section, mapped with ATLAS V, with a resolution of 3 nm/px. This was done with a stage bias energy of 5 kV, allowing for a landing energy of 1.75 keV, and at a working distance of 3.25 mm.

Stitching & registration. Stitching and registration were modelled after published methods[41], employing render (https://github.com/saalfeldlab/render) to store transformations of individual images, and custom python code (https://github.com/AllenInstitute/render-python-apps/blob/master/renderapps/cross_modal_registration) that helped create TrakEM2 projects for each section to be set up. Within the projects, each section was stitched, roughly registered for each multiplexed section, then hand-registered using correspondences between the PSD-95 imagery and synapses seen in the SEM channel. After registration, upsampled IF and EM imagery were exported from TrakEM2 and saved as individual TIFF files. A smaller volume (ROI1: 12.1 x 12.1 x 2.6 μm) was cut out and aligned across sections with the MultiStackReg plugin, (Brad Busse) in FIJI[127], using the SEM channel. The resulting transformations were then applied to the other channels. This small volume including the SEM channel and all the IF channels was uploaded to webKnossos[153] to be analyzed as a conjugate IF-SEM volume.

Image processing of the conjugate IF-SEM dataset. For the fluorescence channels, background was subtracted using the Subtract Background function in FIJI, with a rolling ball radius of 500. Images were normalized using the Enhance Contrast function, setting the saturated pixels at 0.01%. The SEM images were adjusted in FIJI by converting to 32 bit and applying an Unsharp mask (radius 2, mask weight 0.7). Contrast was enhanced using the Enhance Contrast function with saturated pixels at 0.02%, followed by gamma adjustment to 1.2, and Unsharp mask (radius 1, mask weight 0.4). The processed images were finally reverted back to 8 bit. These image processing steps were applied before further analysis of the conjugate dataset.

Conjugate dataset annotation. Excitatory synapses were annotated in webKnossos using the "Segments tool". Synapses were identified by ultrastructural features, such as the accumulation of presynaptic vesicles apposed to a postsynaptic thickening. In cases of uncertainty, immunofluorescence for PSD-95 was used to assist the identification of *en face* synapses, and immunofluorescence for GABA to distinguish between excitatory and inhibitory synapses. An 80-pixel brush (corresponding to 27 nm) was used to paint over the postsynaptic density of each synapse in the dataset as seen on the serial sections through that synapse. The annotation of each synapse was allocated a separate ID number as an individual segment.

Automated detection of glutamatergic synapses. Glutamatergic synapses were detected in fully aligned and registered multichannel AT volume images using previously described synapse detection software[64,150]. Though PSD-95 is thought to be present at all, or nearly all, glutamatergic synapses[154], it is also detectable at many obviously non-synaptic sites. PSD-95 can therefore be considered necessary but not sufficient when identifying synapses in our multiplex images. We therefore added a second requirement that fluorescence also be elevated for the presynaptic bouton marker synapsin (see antibody table) adjacent to the PSD-95 punctum, to distinguish synapses from non-synaptic PSD-95 puncta. To further guard against misinterpretation of any non-synaptic fluorescence, we required that putative post-synaptic PSD-95 puncta persist in at least two adjacent sections, since synaptic puncta will

almost always extend beyond the bounds of a single 70 nm thin section. The output of this detection process is a probability image where the value of each voxel reflects the probability that it belongs to a glutamatergic synapse. Using manually annotated synapses in the SEM channel as a baseline, we set the probability threshold at 0.75 to minimize false positives. We then merged adjacent suprathreshold voxels to define a continuous detection volume for each synapse and assigned that synapse an integer index.

Analysis of synaptic measurements. To measure the IF signal associated with manually-annotated synapses in the conjugate IF-SEM dataset, the synapse annotations were expanded by 160 pixels (54 nm) on each side, creating a 3-D mask that typically spanned several serial sections for each synapse. The summed and the averaged signal intensity of each IF channel were computed using this mask. Synapse size was estimated in the conjugate IF-SEM dataset using the synapse contact area, calculated as the length of the postsynaptic density on each section through the synapse in the SEM channel, multiplied by the section thickness (70 nm).

For the IF-only dataset, sums and mean values of each IF channel for all voxels within the synapse detections were tabulated with one row per detection index. Synapse size in the IF-only dataset was estimated as the sum of PSD-95 immunofluorescence within the synapse detection volume as determined with the synapse detector described above. This synapse size estimate was validated using the conjugate IF-SEM dataset, which showed a strong linear relationship between synapse contact area (the ultrastructural postsynaptic density in the SEM channel and the summed PSD-95 immunofluorescence within the expanded annotation mask, Figure 2C).

For both datasets, fluorescence values were pre-processed by first trimming outliers, excluded by criteria of lower bound < Q5 – (1.5 * (Q95 – Q5)) and upper bound > Q95 + (1.5 * (Q95 – Q5)), where Q5 is the 5th percentile and Q95 is the 95th percentile value for each channel. Clustering was performed after applying a log transformation to each fluorescence channel and a square-root transformation to the size; outliers were trimmed after transformation. Each column was then z-scored (Python SciKit `StandardScaler`). Clustering was performed using the Ward method and Euclidean metric (Python Seaborn `ClusterMap` function). Silhouette analysis was based on K-means clustering with a range of 2-20 clusters (Python sk-learn `KMeans`) and subsequent silhouette analysis (Python `sk-learn.metrics silhouette_score`). Dendrograms were generated using linkage analysis (Python `Seaborn ClusterMap.Dendrogram` function). UMAPs were calculated using default settings (conjugate dataset) or by enforcing a set number of neighbors (200) and minimum distance (0.25) (Python sk-learn `UMAP` function). UMAP plots were based on 8 values: synapse size, mean fluorescence in the PSD-95, GluA1, GluA2, GluA3, GluA4, GluN1, and GluN2B channels.

In the conjugate IF-SEM dataset, the postsynaptic targets of synapses were classified as soma, dendritic shaft, dendritic spine or axon initial segment, based on their ultrastructure. Three morphologically-defined populations of spines were analyzed: 1) “classical” spines: spines with a well-defined spine head and spine apparatus, that have characteristics typical of a strong synapse, including a perforated postsynaptic density and presynaptic mitochondria; 2) thick-necked spines: large spines with a head diameter ≥ 250 nm and neck diameter ≥ 180 nm; and 3) small spines with a head diameter < 250 nm. GABA-positive dendrites were identified by the presence of GABA-immunofluorescence and lack of spines.

In the IF-only dataset, to identify a population of synapses preferentially targeting GABA dendrites, we used the fluorescence in the GABA channel in the area surrounding the synapse.

To calculate this, we dilated the synapse detection area by 6 pixels in each direction. We then selected the top 2% of synapses by GABA content.

To calculate similarity scores across synapse subclasses (Figure 7), data were first restricted to the same set of variables used to generate UMAP plots. We then subdivided synapses based on groupings including: all synapses; putative GABA-targeting synapses (defined above); putative glutamate-targeting synapses (non-GABA); GABA- and -glutamate-targeting mix of synapses shared postsynaptic target; shared presynaptic target; shared postsynaptic target restricted to targeting putative glutamatergic neurons; shared postsynaptic target restricted to targeting putative GABAergic neurons; synapses formed onto large (classical) spines; synapses formed onto thick-necked spines; and synapses formed onto small spines. We calculated the divergence in size and receptor content by comparing each synapse to every other synapse within the same group using linear Euclidean distance (Python `numpy` package `linalg.norm` function) on the z-scored data.

Code availability. All code associated with this study is available online at github.com/aksimhal/single-synapse-proteomics.

References

1. Schikorski, T. & Stevens, C. F. Quantitative ultrastructural analysis of hippocampal excitatory synapses. *J Neurosci* **17**, 5858–5867 (1997).
2. Schikorski, T. & Stevens, C. F. Quantitative fine-structural analysis of olfactory cortical synapses. *Proc Natl Acad Sci U S A* **96**, 4107–4112 (1999).
3. Holderith, N., Heredi, J., Kis, V. & Nusser, Z. A High-Resolution Method for Quantitative Molecular Analysis of Functionally Characterized Individual Synapses. *Cell Rep* **32**, 107968 (2020).
4. Holderith, N. *et al.* Release probability of hippocampal glutamatergic terminals scales with the size of the active zone. *Nat Neurosci* **15**, 988–997 (2012).
5. O'Rourke, N. A., Weiler, N. C., Micheva, K. D. & Smith, S. J. Deep molecular diversity of mammalian synapses: why it matters and how to measure it. *Nat Rev Neurosci* **13**, 365–379 (2012).
6. Murthy, V. N., Schikorski, T., Stevens, C. F. & Zhu, Y. Inactivity produces increases in neurotransmitter release and synapse size. *Neuron* **32**, 673–682 (2001).
7. Harris, K. M. & Stevens, J. K. Dendritic spines of rat cerebellar Purkinje cells: serial electron microscopy with reference to their biophysical characteristics. *J Neurosci* **8**, 4455–4469 (1988).
8. Harris, K. M. & Stevens, J. K. Dendritic spines of CA 1 pyramidal cells in the rat hippocampus: serial electron microscopy with reference to their biophysical characteristics. *J Neurosci* **9**, 2982–2997 (1989).
9. Murthy, V. N., Sejnowski, T. J. & Stevens, C. F. Heterogeneous release properties of visualized individual hippocampal synapses. *Neuron* **18**, 599–612 (1997).
10. Micheva, K. D., Busse, B., Weiler, N. C., O'Rourke, N. & Smith, S. J. Single-Synapse Analysis of a Diverse Synapse Population: Proteomic Imaging Methods and Markers. *Neuron* **68**, 639–653 (2010).
11. Nusser, Z. Creating diverse synapses from the same molecules. *Curr Opin Neurobiol* **51**, 8–15 (2018).
12. Kharazia, V. N. & Weinberg, R. J. Immunogold localization of AMPA and NMDA receptors in somatic sensory cortex of albino rat. *J Comp Neurol* **412**, 292–302 (1999).
13. van Oostrum, M. & Schuman, E. M. Understanding the molecular diversity of synapses. *Nat Rev Neurosci* (2024) doi:10.1038/s41583-024-00888-w.
14. Nicoll, R. A., Kauer, J. A. & Malenka, R. C. The current excitement in long-term potentiation. *Neuron* **1**, 97–103 (1988).
15. Barco, A., Bailey, C. H. & Kandel, E. R. Common molecular mechanisms in explicit and implicit memory. *J Neurochem* **97**, 1520–1533 (2006).
16. Sjöström, P. J., Rancz, E. A., Roth, A. & Häusser, M. Dendritic excitability and synaptic plasticity. *Physiol Rev* **88**, 769–840 (2008).
17. Mayford, M., Siegelbaum, S. A. & Kandel, E. R. Synapses and memory storage. *Cold Spring Harb Perspect Biol* **4**, a005751 (2012).
18. Frémaux, N. & Gerstner, W. Neuromodulated Spike-Timing-Dependent Plasticity, and Theory of Three-Factor Learning Rules. *Front Neural Circuits* **9**, 85 (2015).
19. Brzosko, Z., Zannone, S., Schultz, W., Clopath, C. & Paulsen, O. Sequential neuromodulation of Hebbian plasticity offers mechanism for effective reward-based navigation. *Elife* **6**, e27756 (2017).
20. Nicoll, R. A. A Brief History of Long-Term Potentiation. *Neuron* **93**, 281–290 (2017).

21. Diering, G. H. & Huganir, R. L. The AMPA Receptor Code of Synaptic Plasticity. *Neuron* **100**, 314–329 (2018).
22. Brzosko, Z., Mierau, S. B. & Paulsen, O. Neuromodulation of Spike-Timing-Dependent Plasticity: Past, Present, and Future. *Neuron* **103**, 563–581 (2019).
23. Magee, J. C. & Grienberger, C. Synaptic Plasticity Forms and Functions. *Annu Rev Neurosci* **43**, 95–117 (2020).
24. Bicknell, B. A. & Häusser, M. A synaptic learning rule for exploiting nonlinear dendritic computation. *Neuron* **109**, 4001-4017.e10 (2021).
25. Jain, A. *et al.* Dendritic, delayed, and stochastic CaMKII activation underlies behavioral time scale plasticity in CA1 synapses. *bioRxiv* 2023.08.01.549180 (2023) doi:10.1101/2023.08.01.549180.
26. Xiao, K., Li, Y., Chitwood, R. A. & Magee, J. C. A critical role for CaMKII in behavioral timescale synaptic plasticity in hippocampal CA1 pyramidal neurons. *Sci Adv* **9**, eadi3088 (2023).
27. Li, G., McLaughlin, D. W. & Peskin, C. S. A biochemical description of postsynaptic plasticity-with timescales ranging from milliseconds to seconds. *Proc Natl Acad Sci U S A* **121**, e2311709121 (2024).
28. Nicoll, R. A. & Schulman, H. Synaptic memory and CaMKII. *Physiol Rev* **103**, 2877–2925 (2023).
29. Cizeron, M. *et al.* A brainwide atlas of synapses across the mouse life span. *Science* **369**, 270–275 (2020).
30. Südhof, T. C. Towards an Understanding of Synapse Formation. *Neuron* **100**, 276–293 (2018).
31. Qi, C., Luo, L.-D., Feng, I. & Ma, S. Molecular mechanisms of synaptogenesis. *Front Synaptic Neurosci* **14**, 939793 (2022).
32. Wang, L. *et al.* A cross-species proteomic map reveals neoteny of human synapse development. *Nature* **622**, 112–119 (2023).
33. Kaizuka, T. *et al.* Remodeling of the postsynaptic proteome in male mice and marmosets during synapse development. *Nat Commun* **15**, 2496 (2024).
34. Petralia, R. S., Sans, N., Wang, Y.-X. & Wenthold, R. J. Ontogeny of postsynaptic density proteins at glutamatergic synapses. *Mol Cell Neurosci* **29**, 436–452 (2005).
35. Sorokina, O. *et al.* A unified resource and configurable model of the synapse proteome and its role in disease. *Sci Rep* **11**, 9967 (2021).
36. Bayés, A. *et al.* Characterization of the proteome, diseases and evolution of the human postsynaptic density. *Nat Neurosci* **14**, 19–21 (2011).
37. Henstridge, C. M., Pickett, E. & Spires-Jones, T. L. Synaptic pathology: A shared mechanism in neurological disease. *Ageing Res Rev* **28**, 72–84 (2016).
38. Lepeta, K. *et al.* Synaptopathies: synaptic dysfunction in neurological disorders - A review from students to students. *J Neurochem* **138**, 785–805 (2016).
39. Grant, S. G. N. Synapse diversity and synaptome architecture in human genetic disorders. *Hum Mol Genet* **28**, R219–R225 (2019).
40. Nugent, F. S., Kirkwood, A., Lupica, C. R. & Sjöström, P. J. Editorial: The synaptic basis of neuropathology. *Front Synaptic Neurosci* **14**, 1043480 (2022).
41. Collman, F. *et al.* Mapping synapses by conjugate light-electron array tomography. *J Neurosci* **35**, 5792–5807 (2015).
42. Micheva, K. D. & Smith, S. J. Array tomography: a new tool for imaging the molecular architecture and ultrastructure of neural circuits. *Neuron* **55**, 25–36 (2007).

43. Smith, S. J. Q&A: Array tomography. *BMC Biol* **16**, 98 (2018).
44. Bloss, E. B. *et al.* Structured Dendritic Inhibition Supports Branch-Selective Integration in CA1 Pyramidal Cells. *Neuron* **89**, 1016–1030 (2016).
45. Argañaraz, C. V., Adjimann, T. S., Perissinotti, P. P. & Soiza-Reilly, M. Selective refinement of glutamate and GABA synapses on dorsal raphe 5-HT neurons during postnatal life. *Development* **149**, dev201121 (2022).
46. Kislinger, G. *et al.* Neurons on tape: Automated Tape Collecting Ultramicrotomy-mediated volume EM for targeting neuropathology. *Methods Cell Biol* **177**, 125–170 (2023).
47. Britz, S. *et al.* Array tomography of in vivo labeled synaptic receptors. *Methods Cell Biol* **187**, 139–174 (2024).
48. Rah, J.-C. *et al.* Thalamocortical input onto layer 5 pyramidal neurons measured using quantitative large-scale array tomography. *Front Neural Circuits* **7**, 177 (2013).
49. Templier, T. MagC, magnetic collection of ultrathin sections for volumetric correlative light and electron microscopy. *Elife* **8**, e45696 (2019).
50. Takamori, S. *et al.* Molecular anatomy of a trafficking organelle. *Cell* **127**, 831–846 (2006).
51. Emes, R. D. & Grant, S. G. N. Evolution of synapse complexity and diversity. *Annu Rev Neurosci* **35**, 111–131 (2012).
52. Koopmans, F. *et al.* SynGO: An Evidence-Based, Expert-Curated Knowledge Base for the Synapse. *Neuron* **103**, 217-234.e4 (2019).
53. Selimi, F., Cristea, I. M., Heller, E., Chait, B. T. & Heintz, N. Proteomic studies of a single CNS synapse type: the parallel fiber/purkinje cell synapse. *PLoS Biol* **7**, e83 (2009).
54. Dharmasri, P. A., Levy, A. D. & Blanpied, T. A. Differential nanoscale organization of excitatory synapses onto excitatory vs. inhibitory neurons. *Proc Natl Acad Sci U S A* **121**, e2315379121 (2024).
55. Holderith, N., Aldahabi, M. & Nusser, Z. Selective Enrichment of Munc13-2 in Presynaptic Active Zones of Hippocampal Pyramidal Cells That Innervate mGluR1α Expressing Interneurons. *Front. Synaptic Neurosci.* **13**, (2022).
56. Smith, S. J. Progress on LTP at hippocampal synapses: a post-synaptic Ca2+ trigger for memory storage? *Trends in Neurosciences* **10**, 142–144 (1987).
57. Hollmann, M. & Heinemann, S. Cloned glutamate receptors. *Annu Rev Neurosci* **17**, 31–108 (1994).
58. Rosenmund, C., Stern-Bach, Y. & Stevens, C. F. The tetrameric structure of a glutamate receptor channel. *Science* **280**, 1596–1599 (1998).
59. McBain, C. J. & Mayer, M. L. N-methyl-D-aspartic acid receptor structure and function. *Physiol Rev* **74**, 723–760 (1994).
60. Traynelis, S. F. *et al.* Glutamate receptor ion channels: structure, regulation, and function. *Pharmacol Rev* **62**, 405–496 (2010).
61. Baude, A., Molnár, E., Latawiec, D., McIlhinney, R. A. & Somogyi, P. Synaptic and nonsynaptic localization of the GluR1 subunit of the AMPA-type excitatory amino acid receptor in the rat cerebellum. *J Neurosci* **14**, 2830–2843 (1994).
62. Nusser, Z. *et al.* Cell type and pathway dependence of synaptic AMPA receptor number and variability in the hippocampus. *Neuron* **21**, 545–559 (1998).
63. Racca, C., Stephenson, F. A., Streit, P., Roberts, J. D. & Somogyi, P. NMDA receptor content of synapses in stratum radiatum of the hippocampal CA1 area. *J Neurosci* **20**, 2512–2522 (2000).
64. Simhal, A. K. *et al.* Probabilistic fluorescence-based synapse detection. *PLoS Comput Biol* **13**, e1005493 (2017).

65. Forrest, D. *et al.* Targeted disruption of NMDA receptor 1 gene abolishes NMDA response and results in neonatal death. *Neuron* **13**, 325–338 (1994).
66. Spruston, N., Jonas, P. & Sakmann, B. Dendritic glutamate receptor channels in rat hippocampal CA3 and CA1 pyramidal neurons. *J Physiol* **482 (Pt 2)**, 325–352 (1995).
67. Nimchinsky, E. A., Yasuda, R., Oertner, T. G. & Svoboda, K. The number of glutamate receptors opened by synaptic stimulation in single hippocampal spines. *J Neurosci* **24**, 2054–2064 (2004).
68. Goncalves, J. *et al.* Nanoscale co-organization and coactivation of AMPAR, NMDAR, and mGluR at excitatory synapses. *Proc Natl Acad Sci U S A* **117**, 14503–14511 (2020).
69. Chen, X. *et al.* Organization of the core structure of the postsynaptic density. *Proc Natl Acad Sci U S A* **105**, 4453–4458 (2008).
70. Takumi, Y., Ramírez-León, V., Laake, P., Rinvik, E. & Ottersen, O. P. Different modes of expression of AMPA and NMDA receptors in hippocampal synapses. *Nat Neurosci* **2**, 618–624 (1999).
71. Kessels, H. W. & Malinow, R. Synaptic AMPA receptor plasticity and behavior. *Neuron* **61**, 340–350 (2009).
72. Hruska, M., Cain, R. E. & Dalva, M. B. Nanoscale rules governing the organization of glutamate receptors in spine synapses are subunit specific. *Nat Commun* **13**, 920 (2022).
73. Paoletti, P., Bellone, C. & Zhou, Q. NMDA receptor subunit diversity: impact on receptor properties, synaptic plasticity and disease. *Nat Rev Neurosci* **14**, 383–400 (2013).
74. Frank, R. A. W. *et al.* NMDA receptors are selectively partitioned into complexes and supercomplexes during synapse maturation. *Nat Commun* **7**, 11264 (2016).
75. Rauner, C. & Köhr, G. Triheteromeric NR1/NR2A/NR2B receptors constitute the major N-methyl-D-aspartate receptor population in adult hippocampal synapses. *J Biol Chem* **286**, 7558–7566 (2011).
76. Tovar, K. R., McGinley, M. J. & Westbrook, G. L. Triheteromeric NMDA receptors at hippocampal synapses. *J Neurosci* **33**, 9150–9160 (2013).
77. Wenthold, R. J., Petralia, R. S., Blahos J, I. I. & Niedzielski, A. S. Evidence for multiple AMPA receptor complexes in hippocampal CA1/CA2 neurons. *J Neurosci* **16**, 1982–1989 (1996).
78. Vardalaki, D., Chung, K. & Harnett, M. T. Filopodia are a structural substrate for silent synapses in adult neocortex. *Nature* **612**, 323–327 (2022).
79. Kubota, Y., Hatada, S. N. & Kawaguchi, Y. Important factors for the three-dimensional reconstruction of neuronal structures from serial ultrathin sections. *Front Neural Circuits* **3**, 4 (2009).
80. Gulyás, A. I., Megías, M., Emri, Z. & Freund, T. F. Total number and ratio of excitatory and inhibitory synapses converging onto single interneurons of different types in the CA1 area of the rat hippocampus. *J Neurosci* **19**, 10082–10097 (1999).
81. Geiger, J. R. *et al.* Relative abundance of subunit mRNAs determines gating and Ca2+ permeability of AMPA receptors in principal neurons and interneurons in rat CNS. *Neuron* **15**, 193–204 (1995).
82. Isaac, J. T. R., Ashby, M. C. & McBain, C. J. The role of the GluR2 subunit in AMPA receptor function and synaptic plasticity. *Neuron* **54**, 859–871 (2007).
83. Leranth, C., Szeidemann, Z., Hsu, M. & Buzsáki, G. AMPA receptors in the rat and primate hippocampus: a possible absence of GluR2/3 subunits in most interneurons. *Neuroscience* **70**, 631–652 (1996).

84. Svoboda, K., Tank, D. W. & Denk, W. Direct measurement of coupling between dendritic spines and shafts. *Science* **272**, 716–719 (1996).
85. Noguchi, J., Matsuzaki, M., Ellis-Davies, G. C. R. & Kasai, H. Spine-neck geometry determines NMDA receptor-dependent Ca2+ signaling in dendrites. *Neuron* **46**, 609–622 (2005).
86. Tønnesen, J., Katona, G., Rózsa, B. & Nägerl, U. V. Spine neck plasticity regulates compartmentalization of synapses. *Nat Neurosci* **17**, 678–685 (2014).
87. Harnett, M. T., Makara, J. K., Spruston, N., Kath, W. L. & Magee, J. C. Synaptic amplification by dendritic spines enhances input cooperativity. *Nature* **491**, 599–602 (2012).
88. Beaulieu-Laroche, L. & Harnett, M. T. Dendritic Spines Prevent Synaptic Voltage Clamp. *Neuron* **97**, 75-82.e3 (2018).
89. Trachtenberg, J. T. *et al.* Long-term in vivo imaging of experience-dependent synaptic plasticity in adult cortex. *Nature* **420**, 788–794 (2002).
90. Grutzendler, J., Kasthuri, N. & Gan, W.-B. Long-term dendritic spine stability in the adult cortex. *Nature* **420**, 812–816 (2002).
91. Kasai, H., Matsuzaki, M., Noguchi, J., Yasumatsu, N. & Nakahara, H. Structure-stability-function relationships of dendritic spines. *Trends Neurosci* **26**, 360–368 (2003).
92. Marcus, G., Marblestone, A. & Dean, T. The atoms of neural computation. *Science* **346**, 551–552 (2014).
93. Unterauer, E. M. *et al.* Spatial proteomics in neurons at single-protein resolution. *Cell* **187**, 1785-1800.e16 (2024).
94. Falkovich, R. *et al.* A synaptic molecular dependency network in knockdown of autism- and schizophrenia-associated genes revealed by multiplexed imaging. *Cell Reports* **42**, (2023).
95. Guo, S.-M. *et al.* Multiplexed and high-throughput neuronal fluorescence imaging with diffusible probes. *Nat Commun* **10**, 4377 (2019).
96. Zhu, F. *et al.* Architecture of the Mouse Brain Synaptome. *Neuron* **99**, 781-799.e10 (2018).
97. van Oostrum, M. *et al.* The proteomic landscape of synaptic diversity across brain regions and cell types. *Cell* **186**, 5411-5427.e23 (2023).
98. Kasthuri, N. *et al.* Saturated Reconstruction of a Volume of Neocortex. *Cell* **162**, 648–661 (2015).
99. Delhaye, M. *et al.* Adaptation of Magnified Analysis of the Proteome for Excitatory Synaptic Proteins in Varied Samples and Evaluation of Cell Type-Specific Distributions. *J Neurosci* **44**, e1291232024 (2024).
100. Sorra, K. E. & Harris, K. M. Occurrence and three-dimensional structure of multiple synapses between individual radiatum axons and their target pyramidal cells in hippocampal area CA1. *J Neurosci* **13**, 3736–3748 (1993).
101. Shapson-Coe, A. *et al.* A petavoxel fragment of human cerebral cortex reconstructed at nanoscale resolution. *Science* **384**, eadk4858 (2024).
102. Consortium, T. Mic. *et al.* Functional connectomics spanning multiple areas of mouse visual cortex. 2021.07.28.454025 Preprint at https://doi.org/10.1101/2021.07.28.454025 (2023).
103. Hodge, R. D. *et al.* Conserved cell types with divergent features in human versus mouse cortex. *Nature* (2019) doi:10.1038/s41586-019-1506-7.
104. Gidon, A. *et al.* Dendritic action potentials and computation in human layer 2/3 cortical neurons. *Science* **367**, 83–87 (2020).

105. Kalmbach, B. E. *et al.* h-Channels Contribute to Divergent Intrinsic Membrane Properties of Supragranular Pyramidal Neurons in Human versus Mouse Cerebral Cortex. *Neuron* **100**, 1194-1208.e5 (2018).

106. Beaulieu-Laroche, L. *et al.* Enhanced Dendritic Compartmentalization in Human Cortical Neurons. *Cell* **175**, 643-651.e14 (2018).

107. Verhoog, M. B. *et al.* Layer-specific cholinergic control of human and mouse cortical synaptic plasticity. *Nat Commun* **7**, 12826 (2016).

108. Weiler, N. C., Collman, F., Vogelstein, J. T., Burns, R. & Smith, S. J. Synaptic molecular imaging in spared and deprived columns of mouse barrel cortex with array tomography. *Sci Data* **1**, 140046 (2014).

109. Simhal, A. K. *et al.* A Computational Synaptic Antibody Characterization Tool for Array Tomography. *Front Neuroanat* **12**, 51 (2018).

110. Micheva, K. D. *et al.* Developing a Toolbox of Antibodies Validated for Array Tomography-Based Imaging of Brain Synapses. *eNeuro* **10**, ENEURO.0290-23.2023 (2023).

111. Kang, J. *et al.* Multiplexed expansion revealing for imaging multiprotein nanostructures in healthy and diseased brain. *Nat Commun* **15**, 9722 (2024).

112. Ku, T. *et al.* Multiplexed and scalable super-resolution imaging of three-dimensional protein localization in size-adjustable tissues. *Nat Biotechnol* **34**, 973–981 (2016).

113. Park, J. *et al.* Epitope-preserving magnified analysis of proteome (eMAP). *Sci Adv* **7**, eabf6589 (2021).

114. Shen, F. Y. *et al.* Light microscopy based approach for mapping connectivity with molecular specificity. *Nat Commun* **11**, 4632 (2020).

115. Holler, S., Köstinger, G., Martin, K. A. C., Schuhknecht, G. F. P. & Stratford, K. J. Structure and function of a neocortical synapse. *Nature* **591**, 111–116 (2021).

116. Lycas, M. D. & Manley, S. DNA-PAINT adaptors make for efficient multiplexing. *Cell Rep Methods* **4**, 100801 (2024).

117. Fiala, J. C., Spacek, J. & Harris, K. M. Dendrite structure. in *Dendrites* (eds. Stuart, G., Spruston, N. & Häusser, M.) 0 (Oxford University Press, 2007). doi:10.1093/acprof:oso/9780198566564.003.0001.

118. Svoboda, K., Tank, D. W. & Denk, W. Direct measurement of coupling between dendritic spines and shafts. *Science* **272**, 716–719 (1996).

119. Zecevic, D. Electrical properties of dendritic spines. *Biophys J* **122**, 4303–4315 (2023).

120. Liao, D., Hessler, N. A. & Malinow, R. Activation of postsynaptically silent synapses during pairing-induced LTP in CA1 region of hippocampal slice. *Nature* **375**, 400–404 (1995).

121. Isaac, J. T., Nicoll, R. A. & Malenka, R. C. Evidence for silent synapses: implications for the expression of LTP. *Neuron* **15**, 427–434 (1995).

122. Kerchner, G. A. & Nicoll, R. A. Silent synapses and the emergence of a postsynaptic mechanism for LTP. *Nat Rev Neurosci* **9**, 813–825 (2008).

123. Zhang, Y., Cudmore, R. H., Lin, D.-T., Linden, D. J. & Huganir, R. L. Visualization of NMDA receptor-dependent AMPA receptor synaptic plasticity in vivo. *Nat Neurosci* **18**, 402–407 (2015).

124. Dobrunz, L. E. Long-term potentiation and the computational synapse. *Proc Natl Acad Sci U S A* **95**, 4086–4088 (1998).

125. Montgomery, J. M. & Madison, D. V. State-dependent heterogeneity in synaptic depression between pyramidal cell pairs. *Neuron* **33**, 765–777 (2002).

126. Montgomery, J. M. & Madison, D. V. Discrete synaptic states define a major mechanism of synapse plasticity. *Trends Neurosci* **27**, 744–750 (2004).

127. O'Connor, D. H., Wittenberg, G. M. & Wang, S. S.-H. Graded bidirectional synaptic plasticity is composed of switch-like unitary events. *Proc Natl Acad Sci U S A* **102**, 9679–9684 (2005).

128. Petersen, C. C., Malenka, R. C., Nicoll, R. A. & Hopfield, J. J. All-or-none potentiation at CA3-CA1 synapses. *Proc Natl Acad Sci U S A* **95**, 4732–4737 (1998).

129. Philpot, B. D. & Bear, M. F. Synaptic plasticity in an altered state. *Neuron* **33**, 665–667 (2002).

130. Chen, X. *et al.* PSD-95 family MAGUKs are essential for anchoring AMPA and NMDA receptor complexes at the postsynaptic density. *Proc Natl Acad Sci U S A* **112**, E6983-6992 (2015).

131. Feng, Y. & Brunel, N. Storage capacity of networks with discrete synapses and sparsely encoded memories. *Phys Rev E* **105**, 054408 (2022).

132. Feng, Y. & Brunel, N. Attractor neural networks with double well synapses. *PLoS Comput Biol* **20**, e1011354 (2024).

133. Satel, J., Trappenberg, T. & Fine, A. Are binary synapses superior to graded weight representations in stochastic attractor networks? *Cogn Neurodyn* **3**, 243–250 (2009).

134. Graves, A. R. *et al.* Visualizing synaptic plasticity in vivo by large-scale imaging of endogenous AMPA receptors. *Elife* **10**, e66809 (2021).

135. Wildenberg, G., Li, H., Sampathkumar, V., Sorokina, A. & Kasthuri, N. Isochronic development of cortical synapses in primates and mice. *Nat Commun* **14**, 8018 (2023).

136. Dorkenwald, S. *et al.* Neuronal wiring diagram of an adult brain. *Nature* **634**, 124–138 (2024).

137. Kuan, A. T. *et al.* Synaptic wiring motifs in posterior parietal cortex support decision-making. *Nature* **627**, 367–373 (2024).

138. Verasztó, C. *et al.* Whole-body connectome of a segmented annelid larva. 2024.03.17.585258 Preprint at https://doi.org/10.1101/2024.03.17.585258 (2024).

139. Witvliet, D. *et al.* Connectomes across development reveal principles of brain maturation. *Nature* **596**, 257–261 (2021).

140. Loomba, S. *et al.* Connectomic comparison of mouse and human cortex. *Science* **377**, eabo0924 (2022).

141. Colonnier, M. Synaptic patterns on different cell types in the different laminae of the cat visual cortex. An electron microscope study. *Brain Research* **9**, 268–287 (1968).

142. Peters, A., Palay, S. L. & Webster, H. deF. *The Fine Structure of the Nervous System: Neurons and Their Supporting Cells*. (Oxford University Press, 1991).

143. Cano-Astorga, N. *et al.* Unambiguous identification of asymmetric and symmetric synapses using volume electron microscopy. *Front. Neuroanat.* **18**, (2024).

144. Eckstein, N. *et al.* Neurotransmitter classification from electron microscopy images at synaptic sites in Drosophila melanogaster. *Cell* **187**, 2574-2594.e23 (2024).

145. Michalska, J. M. *et al.* Imaging brain tissue architecture across millimeter to nanometer scales. *Nat Biotechnol* **42**, 1051–1064 (2024).

146. Shin, T. W. *et al.* Dense, Continuous Membrane Labeling and Expansion Microscopy Visualization of Ultrastructure in Tissues. *bioRxiv* 2024.03.07.583776 (2024) doi:10.1101/2024.03.07.583776.

147. M'Saad, O. *et al.* All-optical visualization of specific molecules in the ultrastructural context of brain tissue. 2022.04.04.486901 Preprint at https://doi.org/10.1101/2022.04.04.486901 (2022).

148. Volk, L., Chiu, S.-L., Sharma, K. & Huganir, R. L. Glutamate synapses in human cognitive disorders. *Annu Rev Neurosci* **38**, 127–149 (2015).

149. Micheva, K. D. *et al.* A large fraction of neocortical myelin ensheathes axons of local inhibitory neurons. *Elife* **5**, e15784 (2016).

150. Simhal, A. K. *et al.* Multifaceted Changes in Synaptic Composition and Astrocytic Involvement in a Mouse Model of Fragile X Syndrome. *Sci Rep* **9**, 13855 (2019).

151. Serafin, R., Gliko, O., Smith, S. J. & Collman, F. MosaicPlanner: Hardware Agnostic Array Tomography Acquisition Software. Preprint at https://doi.org/10.1101/473009 (2018).

152. Schindelin, J. *et al.* Fiji: an open-source platform for biological-image analysis. *Nat Methods* **9**, 676–682 (2012).

153. Boergens, K. M. *et al.* webKnossos: efficient online 3D data annotation for connectomics. *Nat Methods* **14**, 691–694 (2017).

154. Hunt, C. A., Schenker, L. J. & Kennedy, M. B. PSD-95 is associated with the postsynaptic density and not with the presynaptic membrane at forebrain synapses. *J Neurosci* **16**, 1380–1388 (1996).